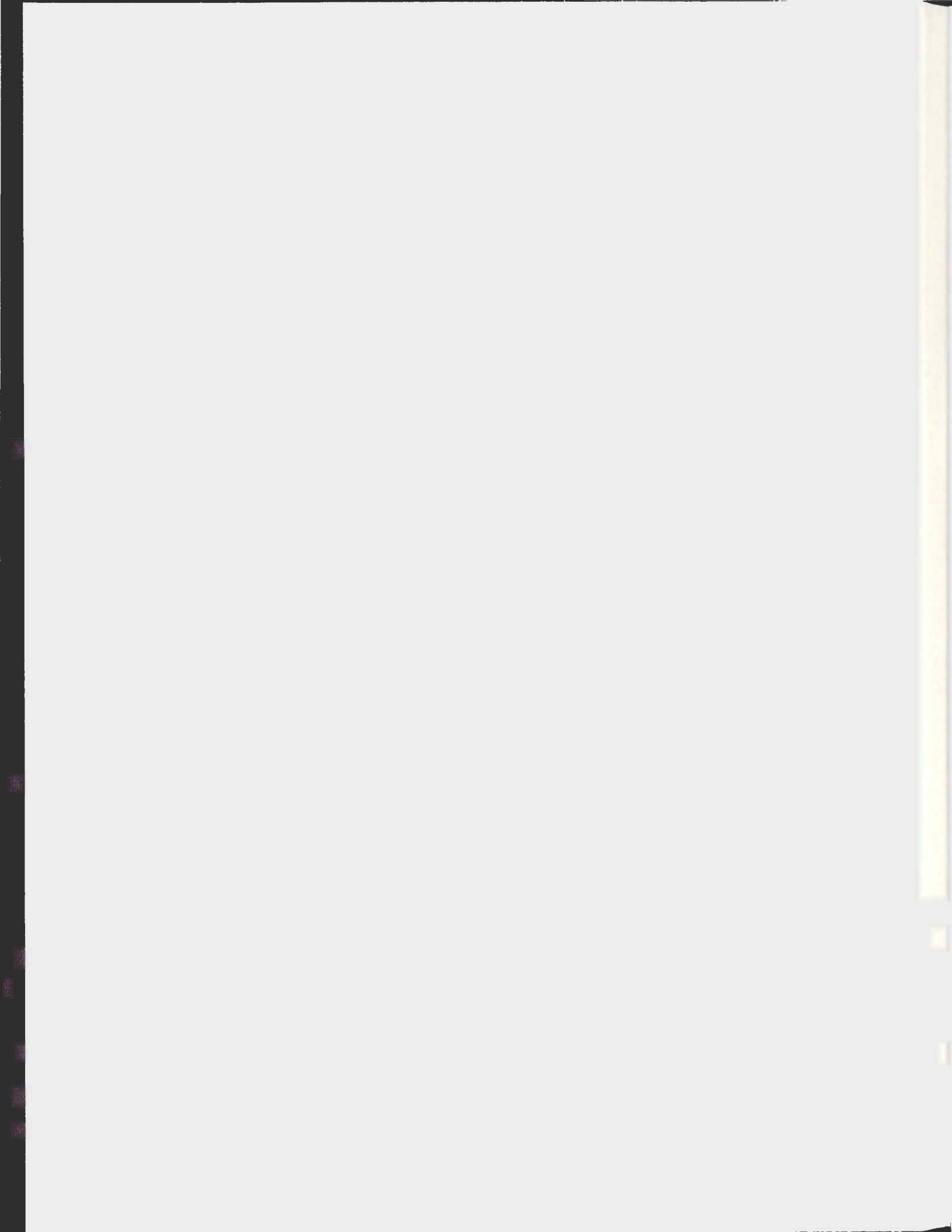


INFERRED BOUNDARY MIXING RATES FROM  
DENSITY INVERSIONS IN THE ST. LAWRENCE ESTUARY

GRAIG SUTHERLAND





# Inferred boundary mixing rates from density inversions in the St. Lawrence Estuary

by

© Graig Sutherland

A thesis submitted to the  
School of Graduate Studies  
in partial fulfilment of the  
requirements for the degree of  
Master of Science

Department of Physics and Oceanography  
Memorial University of Newfoundland

August 2009

## Abstract

When interfacial internal waves shoal over a sloped bottom, a fraction of the wave energy is reflected away while the rest is utilized by such processes as transport, dissipation, and mixing. In this thesis, I investigate the dissipation and mixing parameters inferred from CTD profiles in a region of high shoaling wave activity. This is done by looking at gravitationally unstable portions in the density profiles and sorting them into gravitationally stable ones. The RMS distance the water parcel must travel is referred to as the “Thorpe” scale and this can be used to infer the turbulent dissipation rate and the eddy diffusivity. This method is applied to five days of data, 28 June 2008 to 2 July 2008, obtained off the shore of Ile-aux-Lièvres in the St. Lawrence Estuary. In this region, internal waves predominantly occur between 1 and 3 hours after the local low water during the flood tide. Therefore, the variability of the inferred turbulent and mixing parameters are investigated as a function of tidal phase to determine whether these are concurrent with the increase of shoaling internal waves. The dissipation and mixing parameters associated with a couple of the larger shoaling events are individually presented in higher detail.

# Contents

<b>Abstract</b>	<b>ii</b>
<b>List of Tables</b>	<b>v</b>
<b>List of Figures</b>	<b>vi</b>
<b>1 Introduction</b>	<b>1</b>
1.1 Shoaling Internal Waves . . . . .	2
1.2 Density Overturns and Turbulence . . . . .	3
1.3 St. Lawrence Estuary . . . . .	6
1.4 Thesis Outline . . . . .	10
<b>2 Data and Methods</b>	<b>11</b>
2.1 Sampling . . . . .	11
2.2 ADCP Correction Algorithm: Beam to Earth Transformation . . . . .	13
2.3 Data Reduction . . . . .	17
2.4 Local tide . . . . .	19
<b>3 Overturn Analysis</b>	<b>22</b>

3.1	Theory . . . . .	22
3.2	Limits on Overturn Resolution . . . . .	25
3.3	Detecting Overturns . . . . .	26
3.4	Computing Dissipation Rates . . . . .	28
3.5	Statistical Distribution . . . . .	32
<b>4</b>	<b>Field Observations: Shoaling Events</b>	<b>41</b>
4.1	Internal Solitary Wave Sequence . . . . .	42
4.2	Turbulent Front . . . . .	48
<b>5</b>	<b>Conclusions and Future Work</b>	<b>56</b>
5.1	Summary . . . . .	56
5.2	Future Work . . . . .	58
	<b>Bibliography</b>	<b>60</b>

# List of Tables

2.1	High and low water times for the measured tide at Ile-aux-Liévres. All times are in UTC. . . . .	21
-----	--	----

# List of Figures

1.1	Bathymetric chart of the region near Ile-aux-lièvres in the St. Lawrence Estuary. The red dot denotes where the <i>Lampsilis</i> is typically anchored for the duration of the experiment. The blue dot denotes the location of the moored pT chain. The letters PP in the inset indicate the location of the Pointe-au-Père tidal gauge. The division between the upper estuary, U, and the lower estuary, L, is shown with a black line.	8
1.2	An example of a shoaling ISW on Ile-aux-Lièvres from Bourgault et al. (2007).	9
2.1	Downward facing orientation of the ADCP as viewed from below. Here $\phi_1$ , $\phi_2$ and $\phi_3$ are the heading, pitch and roll angles respectively. The $z$ -axis is upward and is shown going into the page.	14
2.2	Beam orientation in the $y$ - $z$ plane.	15
2.3	Tidal heights recorded at Ile-aux-Lièvres. The thick lines denote the times where there are CTD measurements.	20

3.1	Schematic of a “z-shaped” overturn. The solid line is the gravitationally unstable density profile and the dashed line is the sorted stable profile. The overturn height is denoted by $H$ . . . . .	24
3.2	An overturn which passes both the run-length test and water-mass test. The solid line denotes the raw ctd profile and the dotted line is the profile sorted to be gravitationally stable. . . . .	29
3.3	An overturn which passes the run-length test but not the water-mass test. The solid line denotes the raw ctd profile and the dotted line is the profile sorted to be gravitationally stable. . . . .	30
3.4	Linear fit of $L_O^2 N^3$ vs APEF $N$ . The solid lines denote the range for $a$ of 2.4-4.8. The left panel is the log scale and the right panel is the linear scale. The red line is the linear fit forced through zero with slope $a_0$ and the green line is the linear fit with $a_1$ and $b_1$ as the slope and intercept respectively. The dotted black line shows the slope for $a = 2$ . . . . .	31
3.5	Measured values of $\epsilon$ as a function of tidal phase. The dark black lines denote the times where measurements are available. The values are summed into 30 minute bins. The colour scale is in $\log(\text{W/kg})$ . . . . .	33
3.6	Estimated dissipation rate as a function of hours after LW. The black dotted line denotes the minimum $\epsilon$ resolution of $1.5 \times 10^{-6}$ W/kg. The data is not averaged over time. . . . .	35

3.7	The top panel is a histogram of the number of overturns $N_O$ and the middle panel is the total number of downcasts $N_D$ for each 30 minute bin respectively. Blue denotes all the overturns and red denotes just those where $\epsilon > 1.5 \times 10^{-6}$ W/kg. The bottom panel shows the ratio $N_O/N_D$ . There can be more than one overturn detected per downcast so it is possible for this ratio to exceed one. . . . .	36
3.8	Box and whisker plots of overturn statistics. The top panel shows the Thorpe Scale distribution for each 30 minute bin, the middle panel is the overturn height, and the lower panel shows the available potential energy. The minimum overturn height from (3.6) assuming $\delta z = 0.15$ m is shown with the black dotted line. The red line denotes the median value, the black circle denotes the mean, the blue box encases the data between the 25 <sup>th</sup> and the 75 <sup>th</sup> percentile, and the whiskers go to the outliers. . . . .	37
3.9	Box and whisker plots of turbulent properties. The red line denotes the median value, the black circle denotes the mean, the blue box encases the data between the 25 <sup>th</sup> and the 75 <sup>th</sup> percentile, and the whiskers go to the outliers. The dotted line on the middle panel denotes the theoretical minimum $\epsilon$ of $1.5 \times 10^{-6}$ W/kg. . . . .	38
4.1	The region of ISWs the St. Lawrence Estuary. The red dot denotes the location of the <i>Lampsilis</i> . The black box denotes the inset for all subsequent plots of the echosounder transects. . . . .	42

4.2	Location of each of the echosounder transects associated with Figure 4.3 with the location of the <i>Lampsilis</i> denoted by the red dot. The depth contours denote every 5 m depth interval from 5 to 50 m. . . .	43
4.3	Echosounder images of an approaching internal wave. The red dots denote where the transects pass nearest to the <i>Lampsilis</i> . . . . .	44
4.4	ADCP measurements of a shoaling internal wave on June 29, 2009. The black dots along the top are the downcast locations and the white line is the density contour for $\sigma = 19.4 \text{ kg/m}^3$ . . . . .	45
4.5	Richardson number for a shoaling internal wave on June 29, 2009. The black dots along the top are the downcast locations. The white line is the density contour for $\sigma = 19.4 \text{ kg/m}^3$ . . . . .	46
4.6	Location of each of the echosounder transects associated with Figures 4.7 (top panel) and 4.8 (bottom panel) with the location of the <i>Lampsilis</i> denoted by the red dot. The depth contours denote every 5 m depth interval from 5 to 50 m. . . . .	48
4.7	Echosounder images of an approaching internal wave. The red dots denote where the transects pass closest to the <i>Lampsilis</i> . . . . .	49
4.8	More echosounder images of an approaching internal wave. The red dots denote where the transects pass closest to the <i>Lampsilis</i> . . . .	50

4.9	The top panel shows the turbulent dissipation rate calculated from overturns. The colour scale is in W/kg. The second panel is the density field for 28 June, 2008 and the colour scale is kg/m <sup>3</sup> . The black dots along the top are the downcast locations and the large red dots along the bottom are where the echosounder passes closest to the Lampsilis. The white line is $\sigma = 17.6$ kg/m <sup>3</sup> . . . . .	52
4.10	ADCP measurements and interpolated CTD density field of a shoaling internal wave on June 28, 2009. The black dots along the top are the downcast locations and the large red dots along the bottom are where the echosounder passes closest to the Lampsilis. The white line shows the density contour for $\sigma = 17.6$ kg/m <sup>3</sup> . . . . .	53
4.11	Richardson number for a shoaling internal wave on June 29, 2009. The black dots along the top are the downcast locations. The white line shows the density contour for $\sigma = 17.2$ kg/m <sup>3</sup> . . . . .	54

# Chapter 1

## Introduction

Studies of ocean mixing are largely motivated by the need to parameterize these processes in numerical models that lack the resolution to directly compute the fine and micro-scale mixing processes. Virtually all ocean general circulation models used in studies of climate, biological productivity, and waste disposal must parameterize the effects of mixing averaged over their grid resolution. This requires an understanding of the dynamical processes responsible for the transport and mixing of scalar quantities.

Understanding mixing is also an important aspect in resolving the contradiction between direct measurements of mixing rates being inadequate to provide the stratification observed in the deep ocean against global upwelling associated with deep water formation (Munk and Wunsch 1998). To maintain the equilibrium so the deep ocean doesn't become a stagnant pool of cold salty water, Munk (1966) calculated a mean diapycnal diffusivity of  $10^{-4}$  m<sup>2</sup>/s. Field measurements away from topography calculated a diffusivity of  $10^{-5}$  m<sup>2</sup>/s, which is inadequate and hence the contradiction. Munk (1966) hypothesized that mixing along the boundaries combined with lateral

spreading into the ocean interior may be able to account for the discrepancy. One proposal for this is that breaking internal waves could be a large contributor to boundary mixing (Munk and Wunsch 1998). Breaking internal waves have been shown to contribute significantly to vertical diffusion in lakes (Imberger and Hamblin 1982; Imberger and Ivey 1991; Goudsmit et al. 1997), fjords (Stigebrandt 1979; Farmer and Freeland 1983; Stigebrandt and Aure 1989; Klymak and Gregg 2004) and the continental slope (Wunsch and Hendry 1972; Thorpe et al. 1990; Moum et al. 2003). However, there have been relatively few studies in estuarine environments (Bourgault and Kelley 2003; Bourgault et al. 2008). This thesis aims to expand on previous work (Bourgault and Kelley 2003; Bourgault et al. 2005; Bourgault et al. 2007; Bourgault et al. 2008) to enhance the understanding of mixing in an estuarine environment.

## 1.1 Shoaling Internal Waves

Strongly nonlinear internal solitary waves (ISWs) are a ubiquitous feature of the coastal ocean. They have been observed in moored records, shipboard measurements, and remotely by satellites and shore-based cameras (Sandstrom and Oakey 1995; Bourgault and Kelley 2003; Moum et al. 2003). It is generally believed that ISWs are generated from the interaction of the barotropic tide with variable bottom topography in a stratified fluid. This could be a fjord, or the edge of the continental shelf, or a seamount.

High levels of turbulence are generally associated with ISWs (Sandstrom et al. 1989; Sandstrom and Oakey 1995; Moum et al. 2003; Klymak and Gregg 2004). As

an ISW begins to shoal, i.e. when the wave's amplitude is a significant fraction of the water depth, breaking has been shown to occur as the trailing edge overtakes the wave trough (Vlasenko and Hutter 2002). The shoaling ISW loses energy through turbulent dissipation while the rest is either reflected away or is used to drive mixing and raise the local potential energy (Bourgault et al. 2007). Propagating ISWs also create shear, and depending on the conditions this shear can be great enough to create shear instabilities (also known as Kelvin-Helmholtz instabilities) which are turbulent and will dissipate energy where these instabilities are created so energy dissipation would not be localized to the surf zone where the ISW breaks.

It has also been shown that an ISW of depression may turn into a wave of elevation, also known as a bolus, as it impacts a sloping bottom. This has been observed in the laboratory (Helfrich 1992) as well as in field measurements (Bourgault et al. 2007; Bourgault et al. 2008). Bourgault et al. (2008) found that boluses increased the stratification by bringing dense water up the slope. They hypothesised that boluses may actually reduce boundary turbulence through this process, but their data set was not sufficient to show this conclusively.

## 1.2 Density Overtorns and Turbulence

The length scale of typical turbulent motion in the ocean is small enough (on the order of centimeters) that they require specialized "microstructure" instruments, such as shear probes, for direct. These instruments are not readily available on most oceanographic surveys so there are no estimates of mixing for the vast majority of

oceanographic studies. It has been suggested (Thorpe 1977; Dillon 1982; Galbraith and Kelley 1996; Gargett and Garner 2008) that mixing and dissipation rates can be inferred from coarser “fine-scale” density profiles calculated from CTD (Conductivity - Temperature - Depth) profiles. Dillon (1982) suggested that a key property of mixing is the scale of the overturning eddies, which can be on the order of meters, that can be resolved by readily obtained CTD measurements. These overturning eddies are revealed as “inversions” in the density profiles, i.e. regions of the water column which are gravitationally unstable. This permits the possibility that mixing can be inferred from the broad database of CTD data available.

Mixing parameters are calculated by re-ordering the gravitationally unstable patches so they are stable. Each unstable density measurement must travel a distance within the overturn to become stable. The root mean square (rms) distance of all the density measurements within the overturn is referred to as the “Thorpe Scale”  $L_T$  (Dillon 1982; Peters et al. 1988; Galbraith and Kelley 1996; Gargett and Garner 2008). This re-ordering is often done over an isolated overturn, defined by a region where the sum of the density anomalies between the re-ordered and raw density profiles equalling zero. It has been shown that the Thorpe scale can then be related to the Ozmidov scale  $L_O = (\epsilon/N^3)^{1/2}$  where  $\epsilon$  is the turbulent dissipation rate and  $N$  is the buoyancy frequency (Ozmidov 1965). Therefore, relating  $L_T$  with  $L_O$  can give estimates for the rate of turbulent kinetic energy dissipation.

The turbulent dissipation rate can in turn be related to the eddy diffusivity  $K_\rho = \Gamma\epsilon/N^2$  where  $\Gamma$  is the mixing efficiency. This was derived by Osborn (1980) assuming a steady-state of the turbulent kinetic energy equation where the turbulent production,

i.e. the work done by the Reynolds stress times the mean shear, is balanced by the turbulent dissipation rate,  $\epsilon$ , and the buoyancy production. The ratio of the buoyancy flux to the turbulent production is defined as the flux Richardson number,  $R_f$ , and using this defined the eddy diffusivity  $K_\rho$  to be

$$K_\rho = \frac{R_f \epsilon}{(1 - R_f) N^2}. \quad (1.1)$$

Turbulence in a shear flow occurs when  $R_f$  is below a critical value, which was derived to be 0.15 (Ellison 1957). For  $R_f \leq 0.15$  then (1.1) becomes

$$K_\rho \leq \frac{0.15\epsilon}{0.85N^2} < 0.2 \frac{\epsilon}{N^2}. \quad (1.2)$$

The 0.2 value in (1.2) is referred to as the mixing efficiency,  $\Gamma$ , and is often assumed to be between 0.1 and 0.2 (Moum et al. 2003; Klymak and Gregg 2004; Mirshak 2008).

Good agreement between  $L_O$  and  $L_T$  (Dillon 1982; Peters 1997; Bourgault et al. 2008), but with variations on the value of  $L_O/L_T$  depending on the oceanographic setting. Dillon (1982) found  $L_O/L_T$  to be 0.8 in a study directly measuring turbulence in deepwater and relating  $L_O$  to  $L_T$  within each overturn. However, their measurements, taken in the near surface water, found larger values of  $L_O/L_T$  where the Richardson number is more variable. In a partially mixed estuary, Peters (1997) found  $L_O/L_T = 1.5$  by averaging the Ozmidov and Thorpe length scales over 20 minutes. Bourgault et al. (2008) found a mean value of  $L_O/L_T = 1.6$  by using the depth averaged values for  $L_O$  and  $L_T$  in the St. Lawrence Estuary. However, by computing  $L_T$  for the entire water column, and not for each overturn, will have a tendency to underestimate  $L_T$  and thus increase the ratio of  $L_O/L_T$ . These studies

suggest that  $L_O/L_T > 1$  in shallow more turbulent regions and tends to  $L_O = 0.8L_T$  in deeper more stratified water. It appears likely that  $L_O/L_T > 1$  in this region, yet without direct dissipation estimates it is impossible to determine this on the spatial and timescales of each individual overturn. Therefore,  $L_O/L_T = 1$  will be used, which is consistent with previous work in estimating turbulent dissipation from  $L_T$  (Klymak and Gregg 2004).

The Thorpe scale approach has several limitations. For example, ship heave creates vertical oscillations in the CTD profiler causing it to re-sample the same parcel of water. This prevents profiles from measuring the ocean in its “natural” state. Even variations in the fall speed create non-uniform spatial sampling and make it difficult to adequately resolve overturning regions. There is also the issue of the accuracy of density profiles, which are calculated from the measured conductivity and temperature profiles.

Despite these limitations, Thorpe scales still give good results where the stratification is high ( $N > 0.01 \text{ s}^{-1}$ ) and diffusivities are higher than  $10^{-4} \text{ m}^2/\text{s}$  (Stansfield et al. 2001; Klymak and Gregg 2004). In high stratification even small vertical displacements should correspond to measureable density signals.

### 1.3 St. Lawrence Estuary

The St. Lawrence Estuary, with an area of  $10\,800 \text{ km}^2$ , is a 500 km long estuary located in Québec, Canada that is connected to the Atlantic Ocean vis the Gulf of St. Lawrence (Figure 1.1). The estuary is divided into upper and lower sections by a

sudden change in the bottom topography (Figure 1.1, dotted line denotes division). The upper estuary is defined by being narrower and shallower (2-20 km and less than 100 m respectively) than the wider and deeper upper estuary (20-50 km and greater than 300 m respectively). The bottom topography of the upper estuary is highly variable with several disconnected channels and troughs separated by ridges and islands. The upper estuary is further divided into a north and south channel (Figure 1.1) with the north channel mostly continuous along the upper estuary and the south channel being much shallower with depths less than 10 m (Dickie and Trites 1983; El-Sabah 1988).

This study will focus on the region on the western bank of Ile-aux-Lièvres in the upper estuary. This is a region of high tidal dissipation (Reid 1977) and a prominent location for shoaling internal waves in the estuary (Bourgault et al. 2001; Bourgault and Kelley 2003). An example of the shoaling process of an internal wave on Ile-aux-Lièvres is illustrated in Figure 1.2 (from Bourgault et al. (2007)). As the initial wave of depression shoals, the rear of the wave steepens until by  $t=488$  s it becomes a wave of elevation (bolus). This occurred without any evidence of breaking or overturning, suggesting that these events may not be turbulent features. It was found by Wallace and Wilkinson (1988) that the initial shoaling ISW in their experiments did not break, but breaking always occurred for subsequent shoaling ISWs which interacted with the backflow created by the preceding wave. Although large dissipation rates have been measured in the swash zone of the internal waves (Bourgault et al. 2008) and internal waves have been observed breaking on the shores of Ile-aux-Lièvres (Bourgault et al. 2007). It is still unclear how significant breaking ISWs are to the total energy budget

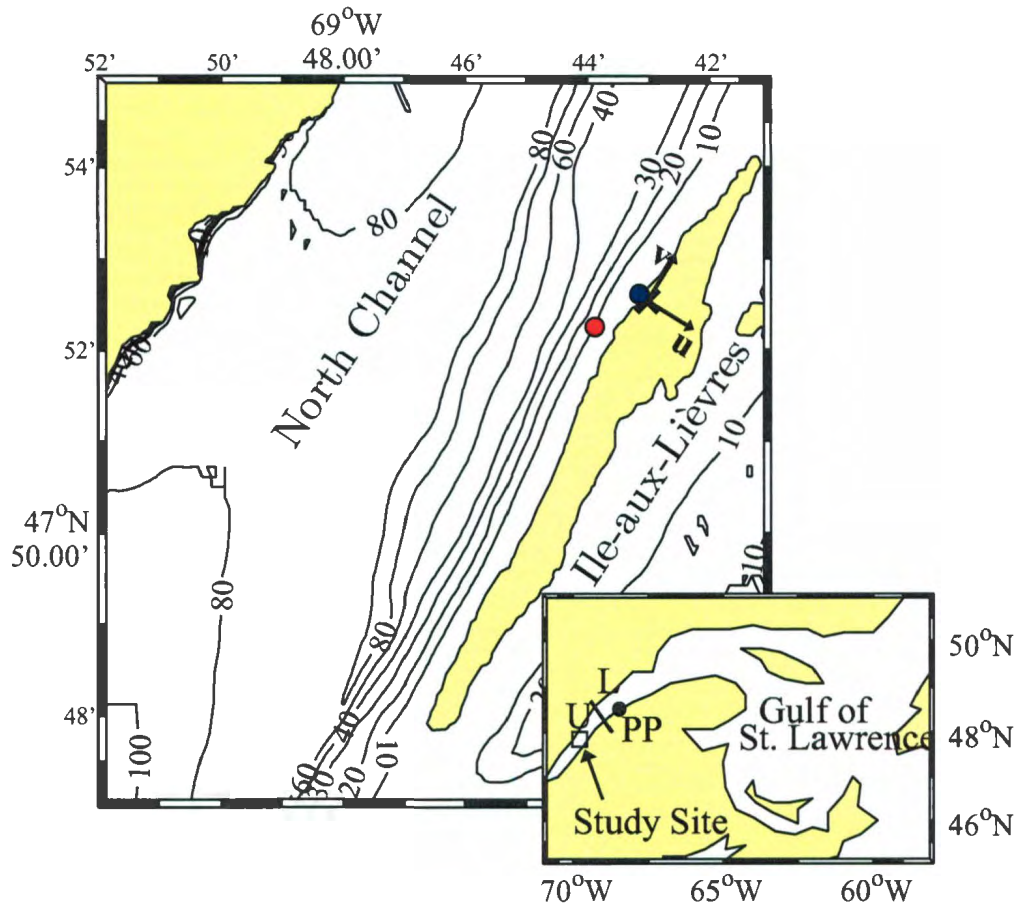


Figure 1.1: Bathymetric chart of the region near Ile-aux-lièvres in the St. Lawrence Estuary. The red dot denotes where the *Lampsilis* is typically anchored for the duration of the experiment. The blue dot denotes the location of the moored pT chain. The letters PP in the inset indicate the location of the Pointe-au-Père tidal gauge. The division between the upper estuary, U, and the lower estuary, L, is shown with a black line.

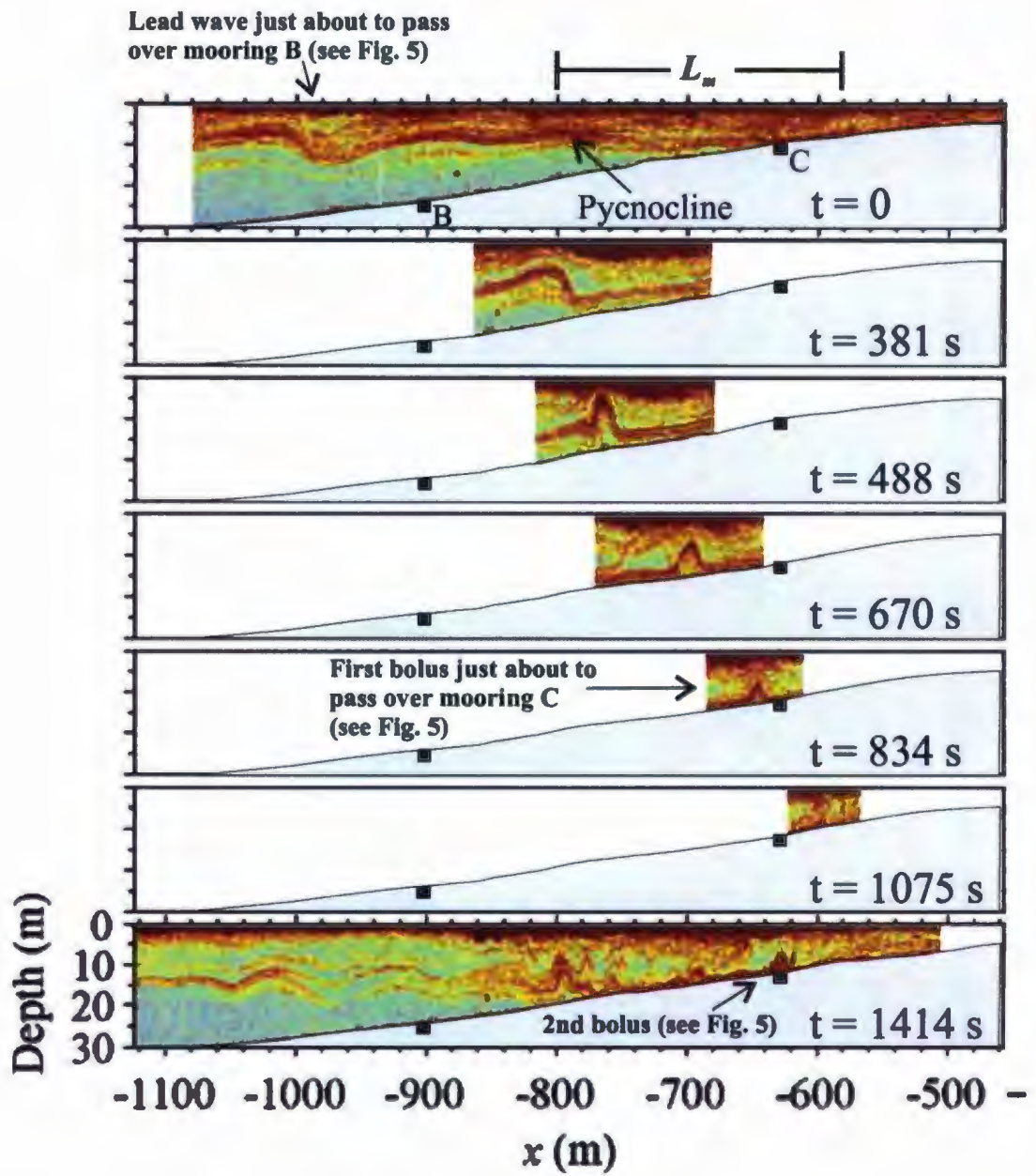


Figure 1.2: An example of a shoaling ISW on Ile-aux-Lièvres from Bourgault et al. (2007).

of the region.

## **1.4 Thesis Outline**

The thesis is outlined as follows. The data available and methods used for analysis are outlined in Chapter 2. Chapter 3 introduces two methods to detect density inversions present in CTD casts. These methods are used to calculate turbulent dissipation rates and are analysed as a function of tidal phase. Chapter 4 investigates two specific internal wave events observed shoaling onto Ile-aux-lièvres. The evolution of the current and density fields, as these shoal onto the beach and how these relate to observed density overturns, will also be shown. A discussion of the results and possible future work is presented in Chapter 5.

# Chapter 2

## Data and Methods

### 2.1 Sampling

Wave-induced boundary processes were examined off the western coast of Ile-aux-Lièvres Island in the St. Lawrence estuary (Figure 1.1). Measurements were carried out aboard the 24 m research vessel *Lampsilis* which was anchored at a water depth of 15 m. Sampling was carried out during every other flood tide between 28 June 2008 and 2 July 2008. The flood tides were chosen to correspond to maximum internal wave activity, which is 2 - 4 hours after low water at Pointe-au-Père (Bourgault and Kelley 2003; Bourgault et al. 2005; Mirshak 2008; Bourgault et al. 2008).

Density profiles inferred from CTD measurements were obtained with a SeaBird Electronics (SBE) *19plus* SEACAT profiler sampling at 4 Hz. The profiles were collected by continuously “yo-yo”-ing the CTD throughout the water column. These “yo-yo” profiles are then sorted into downcasts by taking the samples with the profiler falling and ignoring any pressure reversals due to ship heave.

There were a total of 1411 downcasts collected over the five days of experiments. During the sampling periods there was roughly one downcast every 60 s. Averaged over all the available downcasts, the mean fall speed and standard deviation of the CTD was  $w_{CTD} = 0.62 \pm 0.02$  m/s. Given a sampling rate of 4 Hz, this gives a mean depth resolution  $\delta z = 0.15 \pm 0.01$  m.

Flow visualization and three-dimensional current profiles were obtained with a 1200-kHz ADCP manufactured by RD Industries (RDI). This was mounted to the bottom of the *Lampsilis* between June 28, 2009 to July 2, 2009. The data were recorded for each ping, i.e. there was no ensemble averaging, with a ping-rate of every 2.8 seconds with the exception of July 2 where the ping-rate is 0.4 seconds. The data from the first two days were recorded in ship coordinates, i.e. the velocities are automatically converted to the cartesian axis of the ship, while the final three days are recorded in beam coordinates. Bottom tracking is enabled to correct for ship motion.

The ADCP velocities were recorded in ship coordinates with the aim to calculate Reynolds stresses from the beam variances (Lohrmann et al. 1990; Lu and Lueck 1999b). However, if the rotational movements of the ADCP are not zero this leads to large biases in the beam variance that are not due to the velocity field. Lu and Lueck (1999b) showed that for a  $2^\circ$  rms tilt angle in just the roll, and assuming that the pitch and heading remained constant, that if this perfectly correlates with a  $1 \text{ ms}^{-1}$  current would introduce a bias in the Reynolds stress on the order of  $10^{-3} \text{ m}^2\text{s}^{-2}$ . Given estimates of the mean shear in the region of  $10^{-2} \text{ s}^{-2}$  (Bourgault et al. 2001) this would give a bias in the eddy diffusivity of  $10^{-1} \text{ m}^2\text{s}^{-1}$ , which is much too large

for our purposes here. Even if there was only a correlation value between the pitch and the current of 0.1, the bias in the Reynolds stress would only be an order of magnitude smaller, which is still too large for this region. Lu and Lueck (1999b) also derived the bias in calculating the Reynolds stress from Doppler noise, for a moored ADCP so there is zero rotational movement, was estimated to be  $10^{-5} \text{ m}^2\text{s}^{-2}$ , which would still make it difficult to calculate eddy diffusivities with adequate accuracy. Therefore, ADCP data were only used for velocity profiles and Richardson number calculations.

A Biosonics echosounder was towed from the 8 m research vessel *Merlu* to visualize the small flow features from the acoustic backscatter signal. Transects were performed towards and away from Ile-aux-Lièvres near the anchored *Lampsilis* to track shoaling internal waves as they pass by the ship. The echosounder operates at 120 kHz and averages the backscatter into 0.175 m bins at a sampling rate of 5 Hz.

## 2.2 ADCP Correction Algorithm: Beam to Earth Transformation

The beam geometry for a downward facing RDI ADCP is shown in Figure 2.1. The beams are separated by an angle,  $\theta$ , from their axis and the axis of the beams are orthogonal to one another, i.e. the plane formed by beams 1 and 2 are orthogonal to that of the plane formed by beams 3 and 4. Rotation around the centerline,  $\phi_1$ , defines the heading, while the rotation around the x and y axis defines the pitch,  $\phi_2$ ,

and roll,  $\phi_3$ , respectively.

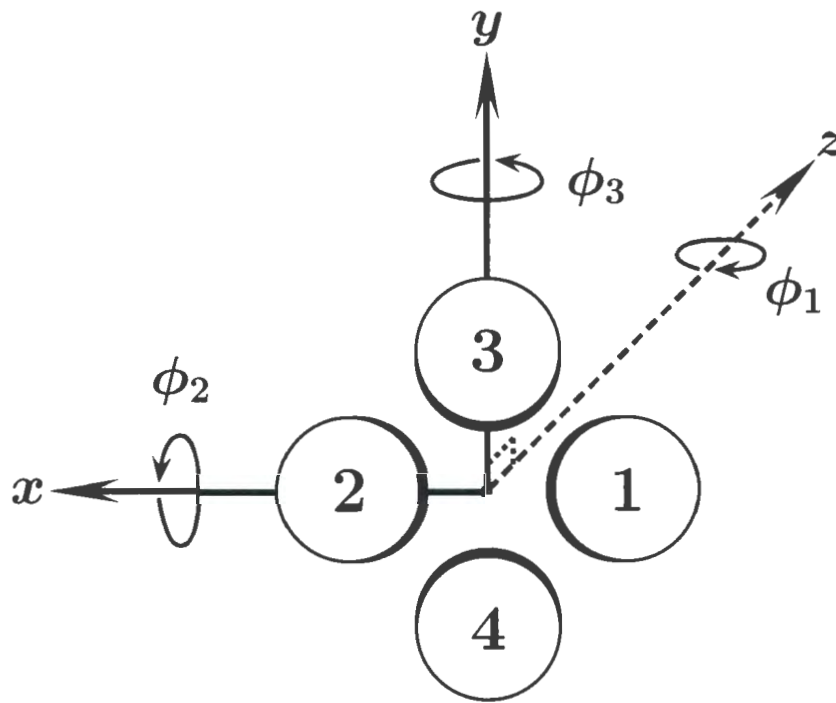


Figure 2.1: Downward facing orientation of the ADCP as viewed from below. Here  $\phi_1$ ,  $\phi_2$  and  $\phi_3$  are the heading, pitch and roll angles respectively. The  $z$ -axis is upward and is shown going into the page.

The velocity vector along each of the four beams,  $b_i$ , where  $i = 1, \dots, 4$  can be expressed in terms of the pitch and roll,  $\phi_2$  and  $\phi_3$ , and the cartesian velocity measured by each beam, i.e.  $u_i$ ,  $v_i$  and  $w_i$  (Lohrmann et al. 1990; Lu and Lueck 1999a). Assuming the pitch and roll are small, i.e.  $\sin \phi \approx \phi$ , to first order the velocities

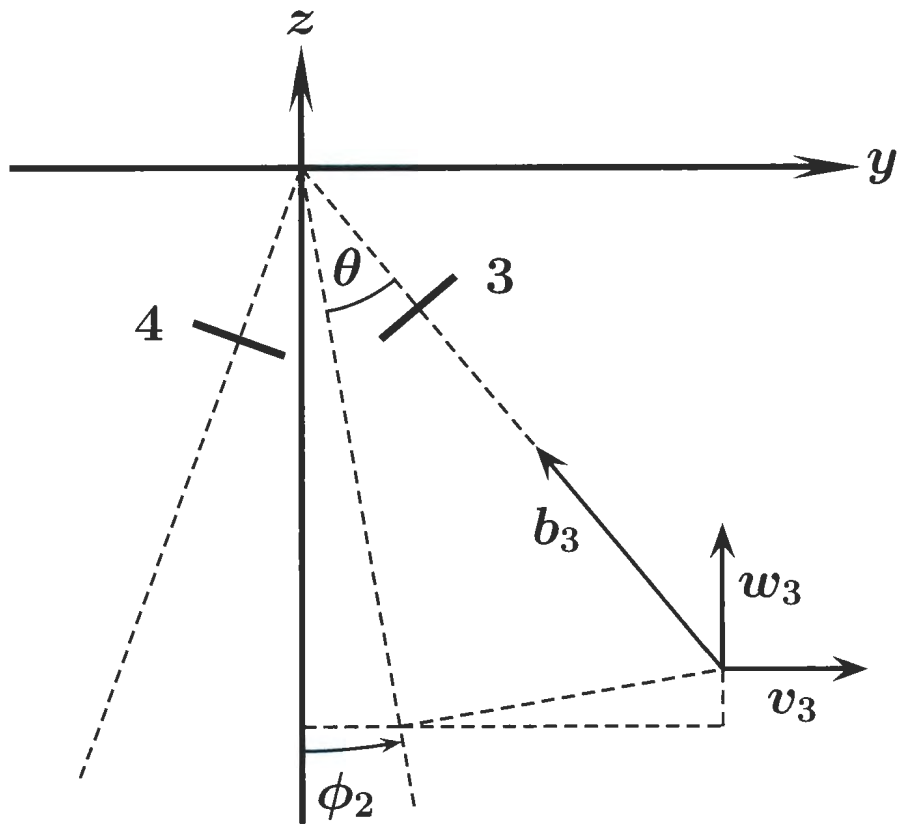


Figure 2.2: Beam orientation in the  $y$ - $z$  plane.

detected by each beam are given as

$$\begin{aligned}
b_1 &= u_1 (\sin \theta + \phi_3 \cos \theta) + w_1 (\cos \theta - \phi_3 \sin \theta) - v_1 \phi_2 \cos \theta, \\
b_2 &= -u_2 (\sin \theta - \phi_3 \cos \theta) + w_2 (\cos \theta + \phi_3 \sin \theta) - v_2 \phi_2 \cos \theta, \\
b_3 &= -v_3 (\sin \theta + \phi_2 \cos \theta) + w_3 (\cos \theta - \phi_2 \sin \theta) + u_3 \phi_3 \cos \theta, \\
b_4 &= v_4 (\sin \theta - \phi_2 \cos \theta) + w_4 (\cos \theta + \phi_2 \sin \theta) + u_4 \phi_3 \cos \theta,
\end{aligned} \tag{2.1}$$

where (2.1) should be rotated by the heading,  $\phi_1$ , to get the eastward and northward velocity components.

From the along beam velocities of (2.1) the “earth coordinate” velocities can be defined to first-order as,

$$\begin{aligned}
\hat{u} &= \frac{b_1 - b_2}{2 \sin \theta} + \phi_3 \frac{b_1 + b_2}{2 \cos \theta}, \\
\hat{v} &= \frac{b_4 - b_3}{2 \sin \theta} - \phi_2 \frac{b_3 + b_4}{2 \cos \theta}, \\
\hat{w} &= \frac{b_1 + b_2 + b_3 + b_4}{4 \cos \theta} - \phi_3 \frac{b_1 - b_2}{2 \sin \theta} + \phi_2 \frac{b_4 - b_3}{2 \sin \theta}, \\
\hat{e} &= \frac{(b_1 + b_2) - (b_3 + b_4)}{4 \cos \theta},
\end{aligned} \tag{2.2}$$

plus an additional compass rotation. This assumes that  $u_i$ ,  $v_i$  and  $w_i$  are horizontally homogeneous between each beam. The ADCP beam angle,  $\theta$ , is  $20^\circ$  so the beam separation at a range of 15 m is roughly 10 m and at a range of 5 m the separation is almost 3.5 m. Therefore, the assumption of spatial homogeneity will break down for flows with length scales smaller than a few meters. However, the mean flow is expected to be spatially homogenous over the separation distance (Lu and Lueck 1999a).

## 2.3 Data Reduction

To reduce random noise in the corrected ADCP current measurements, a fourth-order low-pass Butterworth filter is applied in time and vertical space with cutoff frequencies 1/10 Hz and 1/2 cpm respectively. The velocities are then bi-linearly interpolated onto a  $30 \text{ s} \times 0.5 \text{ m}$  regular grid.

The CTD profiles first need to be corrected for the mismatch between conductivity and temperature profiles. There are two steps involved to correct for this for each downcast. First, the data needs to be corrected for the short-term mismatch of the temperature and conductivity sensors (Lueck and Picklo 1990; Morrison et al. 1994). The temperature and conductivity sensors should match up well if the majority of the variance of conductivity can be explained by the temperature variance. Although this isn't always the case, from visual inspection of many casts where the temperature and conductivity variance were similar, the temperature was found to lag conductivity by 0.5 seconds, consistent with the recommendations for the *SBEplus* (Sea-Bird Electronics 2009). At a sample rate of 4 Hz this is a simple two data point lag applied to all the non-conductivity profiles.

Second, there is a long-term mismatch of the conductivity and temperature sensors, also known as thermal lag, due to the thermal heat inertia stored by the conductivity sensor body as it passes through temperature gradients. To correct for this delayed response of the conductivity sensor, Lueck and Picklo (1990) designed a recursive filter to adjust the conductivity profile. This filter is defined by two variables:  $\alpha$ , the initial amplitude of temperature change for a unit step change in ambient

temperature and  $\tau$ , the  $e$ -folding time of the temperature error. Sea-Bird Electronics recommends using values of  $\alpha = 0.04$  and  $\tau = 7$  s for the SBE19*plus* conductivity sensor pumped at  $0.025 \text{ L s}^{-1}$  (Sea-Bird Electronics 2009). This correction is very small (Lueck and Picklo 1990) and only makes a notable correction in steep temperature gradients.

To determine the background mean density field, the profiles were sorted to be gravitationally stable and averaged over 1 m. However, there is no interpolation of the CTD profiles for calculating overturns. This will be explained in more detail in Chapter 4.

The 1-m averaged density profiles were used to calculate the buoyancy frequency squared,

$$N^2 = \frac{g}{\rho_0} \frac{\partial \bar{\sigma}}{\partial z}, \quad (2.3)$$

where  $g$  is the gravitational acceleration  $9.81 \text{ m/s}^2$ ,  $\rho_0$  is the reference density  $1015 \text{ kg/m}^3$ ,  $\bar{\sigma}$  is the density profile that has been vertically filtered with cutoff wavenumber  $1/2 \text{ cpm}$  to be consistent with the velocity filter, and  $z$  is the upwards vertical coordinate. The vertical gradient of  $\bar{\sigma}$  is calculated using centered differences.

Density  $\sigma$  and buoyancy frequency  $N^2$  were bi-linearly interpolated onto a  $30 \text{ s} \times 0.5 \text{ m}$  regular grid to coincide with the reduced velocity measurements. The Richardson number was calculated from the interpolated density and velocity fields as

$$\text{Ri} = \frac{N^2}{S^2}, \quad (2.4)$$

where

$$S^2 = \left( \frac{\partial u}{\partial z} \right)^2 + \left( \frac{\partial v}{\partial z} \right)^2, \quad (2.5)$$

is the vertical shear squared calculated using centered differences. This can be considered a 2-m scale Richardson number given the vertical filter applied to the velocity and density fields. The Richardson number is often used to indicate stability in the water column. Linear theory dictates that shear instabilities exist when  $Ri < 1/4$  (Miles 1961; Kundu and Cohen 2004). However, this is difficult to apply directly due to a lack of vertical resolution and the spatial averaging of the ADCP (Moum et al. 2003). Instead, the Richardson number is used as a qualitative indicator of stability in the water column.

## 2.4 Local tide

Measurements were taken during the flood tide between June 28 and July 2, 2008 as shown in Figure 2.3. Times at which CTD casts were made are denoted by the thick black lines. Tidal measurements were obtained from a pT-chain moored at 1.8 m depth (Figure 1.1).

Internal waves in this region have a tendency to be phase-locked to the tide and mostly occur 2 to 4 hours after low water, which will be denoted LW + 2 hrs and LW + 4 hrs respectively, at Pointe-au-Père (Bourgault and Kelley 2003; Bourgault et al. 2005), which is roughly one hour before low water at Ile-aux-Lièvres (Canadian Tide and Current Tables 2000). Therefore, internal solitary waves are expected to occur predominantly between LW + 1 and LW + 3 relative to the local tide. A list of the

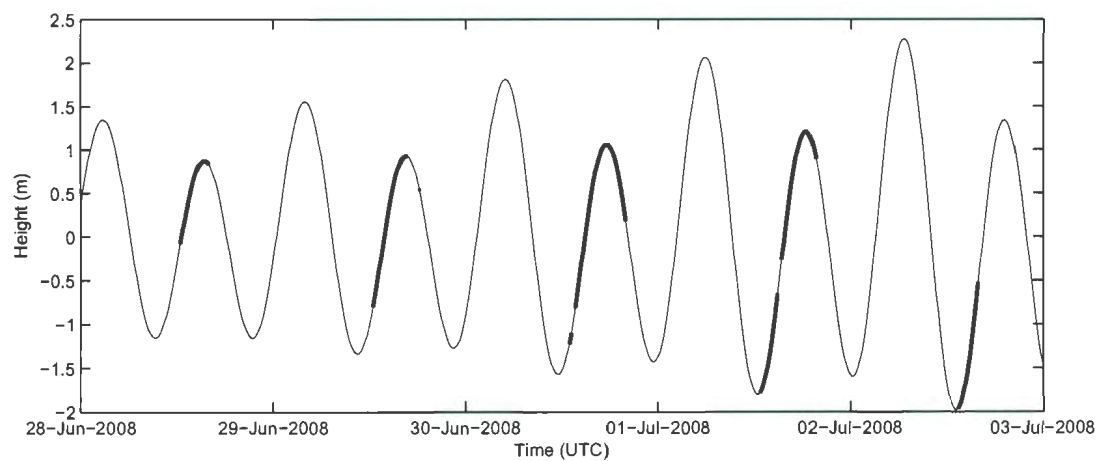


Figure 2.3: Tidal heights recorded at Ile-aux-Lièvres. The thick lines denote the times where there are CTD measurements.

high and low water times are shown in Table 2.1.

Date	Low Water	High Water	Low Water	High Water	Low Water
June 28, 2008		02:48:38	09:18:38	15:23:38	21:28:38
June 29, 2008		03:58:38	10:33:38	16:33:38	22:28:38
June 30, 2008	—	04:58:38	11:33:38	17:38:38	23:28:38
July 1, 2008	—	05:53:38	12:28:38	18:28:38	
July 2, 2008	00:18:38	06:43:38	13:13:38	19:13:38	

Table 2.1: High and low water times for the measured tide at Ile-aux-Liévres. All times are in UTC.

# Chapter 3

## Overturn Analysis

### 3.1 Theory

Mixing parameters can be calculated for gravitationally unstable water patches in one of two ways. The first involves calculating a length scale for the overturning region and relating this to the rate of turbulent kinetic energy dissipation through the Ozmidov length scale (Ozmidov 1965),

$$L_O = \left( \frac{\epsilon}{N^3} \right)^{1/2}, \quad (3.1)$$

where  $\epsilon$  is the turbulent dissipation rate and  $N$  is the mean buoyancy frequency over the inversion. The Ozmidov scale has been found to be related to the overturn scale, also known as the “Thorpe Scale” (Dillon 1982; Peters et al. 1988), which is the rms distance the water needs to travel in an overturn to be gravitationally stable, i.e.

$$L_T = \langle d^2 \rangle^{1/2} \quad (3.2)$$

where  $\langle \rangle$  is an averaging operator and  $d$  is the Thorpe displacement, which is the vertical distance each parcel of water must travel to become gravitationally stable in an unstable profile (Thorpe 1977). Therefore, relating  $L_O$  to  $L_T$ , and knowing the mean stratification  $N$ , can give estimates of  $\epsilon$ . In this study  $L_O \sim L_T$  will be adopted, consistent with previous work which determined dissipation rates from  $L_T$  (Klymak and Gregg 2004). The Thorpe scale can be averaged over any distance, but commonly it's averaged over each individual overturn. This is what is adopted for this study.

A second method to determine  $\epsilon$  is to calculate it from the available potential energy flux (APEF) associated with the Thorpe fluctuation ( Crawford 1986; Galbraith and Kelley 1996). If the turbulent kinetic energy of the overturning region is proportional to available potential energy, and it dissipates on a time scale proportional to the buoyancy period, then the dissipation rate should be

$$\epsilon = a \text{ APEF } N \quad (3.3)$$

where  $a$  is an empirical coefficient measured to be between 2.4 and 4.8 (Crawford 1986). The APEF for a discretely sampled profile is defined as

$$\text{APEF} = \frac{g}{n\rho_0} \sum_{i=1}^n z_i \sigma'_i \quad (3.4)$$

where  $\sigma'_i = \sigma_i - \hat{\sigma}_i$ ,  $\sigma_i$ , and  $\hat{\sigma}_i$  are the Thorpe fluctuation, raw density, and stably sorted density measurements at depth  $z_i$ .

The empirical value of  $a$  may be partially explained theoretically by noting that  $\text{APEF} = N^2 L_T^2 / 2$  for a “z-shaped” overturn in a linearly stratified density field (Figure 3.1). The discrete APEF equation of (3.4) can be written in the continuous form

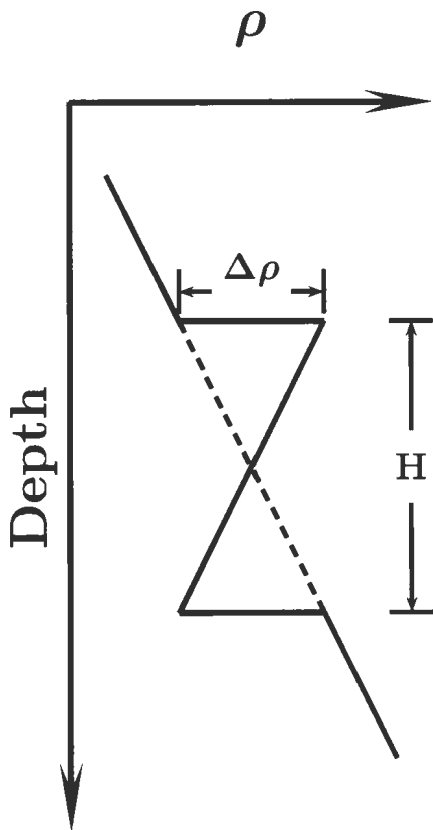


Figure 3.1: Schematic of a “z-shaped” overturn. The solid line is the gravitationally unstable density profile and the dashed line is the sorted stable profile. The overturn height is denoted by  $H$ .

for an overturn of height  $H$ , which would be

$$APEF = \frac{g}{\rho_0} \frac{1}{H} \int_0^H \sigma'_i z dz. \quad (3.5)$$

For the “z-shaped” overturn of Figure 3.1, and substituting  $\sigma'_i = \frac{2\Delta\rho}{H}z - \Delta\rho$  into (3.5) and noting that  $LT^2 = H^2/3$  and  $N^2 = g/\rho_0 \Delta\rho/H$ , gives  $APEF = N^2 L_T^2/2$ .

Assuming  $L_T \sim L_O$  and substituting this into (3.1) gives  $\epsilon \sim 2 APEF N$ , which is very similar to the empirical value found by Crawford (1986).

## 3.2 Limits on Overturn Resolution

The resolution of the CTD imposes a basic constraint on the measurable size of overturns. First, no overturns can be detected below the Nyquist frequency, which is twice the vertical resolution  $\delta z$ . More robust methods can be developed by assuming a minimum number of samples per resolved wavelength (Koch et al. 1983; Levitus 1982). An optimal rule of thumb suggested by Galbraith and Kelley (1996) for the vertical resolution is

$$L_z \approx 5\delta z \quad (3.6)$$

where  $\delta z$  is the vertical spacing of the profile measurements.

Another limit on the vertical resolution is derived from the ability of the profiler to resolve the density inversions of the overturn. The minimum and maximum density of an overturn must be greater than the density resolution,  $\delta\rho$ , of the instrument. Therefore, overturns no smaller than

$$L_\rho \approx 2 \left| \frac{\delta\rho}{\partial\sigma/\partial z} \right| \quad (3.7)$$

can be detected, where  $\partial\sigma/\partial z$  is smoothed over a larger distance than the overturn scale. In terms of the buoyancy frequency, (3.7) is

$$L_\rho \approx 2 \frac{g}{N^2} \frac{\delta\rho}{\rho_0}. \quad (3.8)$$

In an estuarine environment, where  $N = 0.02 \text{ s}^{-1}$  and assuming a CTD density resolution of  $\delta\rho \sim 10^{-3} \text{ kg m}^{-3}$ , gives  $L_\rho \sim 0.05 \text{ m}$ . In this case, detected overturns are more limited by (3.6) than (3.8) assuming  $\delta z > 0.01 \text{ m}$ , which is usually the case with CTD measurements.

Due to the limit on the vertical resolution of the overturn, there is also a limit on the minimum dissipation rate that can be detected. Using (3.1) and assuming the overturn scale equals the Ozmidov scale, Galbraith and Kelley (1996) stated the minimal dissipation rate to be

$$\epsilon_z \approx 25\delta z^2 N^3 \quad (3.9)$$

assuming the minimum vertical resolution of (3.6). However,  $L_T$  is the rms displacement and not the thickness of the overturn. For a linear  $z$ -shaped density overturn,  $L_T$  is related to the overturn thickness  $H$  by  $L_T = H/\sqrt{3}$ . Assuming a minimum overturn thickness of (3.6) then (3.9) will become

$$\epsilon_z \approx \frac{25}{3}\delta z^2 N^3. \quad (3.10)$$

### 3.3 Detecting Overturns

The resolution limits due to overturn thickness (3.6) and dissipation resolution (3.10) provide crude lower bounds to overturn detection. Due to errors in CTD sampling and

the complex nature of overturns it is likely that the actual limits on overturn detection will be much greater. Galbraith and Kelley (1996) devised a way to help ensure that the detected overturns are physical overturns. To avoid false detections from random noise, a “run-length” test is performed which assumes for physical overturns that there will be a “run” of consecutive unstable density anomalies greater than the noise threshold. For a random, uncorrelated time series with equal positive and negative values, the probability density function (PDF) of run length is

$$P(n) = 2^{-n} \quad (3.11)$$

where  $P(n)$  is the probability of a run of length  $n$  consecutive positive or negative anomalies. To test for noise based inversions, the observed PDF of the measured Thorpe fluctuations are compared with (3.11). Furthermore, Galbraith and Kelley (1996) define the minimal run length required for a real density overturn to be the shortest run length at which the observed PDF is double that predicted by (3.11). This doubling factor is empirically determined by Galbraith and Kelley (1996) after visually inspecting many profiles. From all the CTD downcasts between 28 June 2008 and 2 July 2008 it is found that a run-length of 7 consecutive density anomalies is required so that the distribution is greater than double (3.11). There are 414 overturns detected during these five days which pass this.

A further criterion imposed by Galbraith and Kelley (1996) assumed a certain amount of “tightness” in the local T-S space. This is because a parcel of water that is mixed should remain on a straight line in the T-S plane. To test for “tightness”, the density profiles are fitted as linear functions of salinity and temperature, i.e.

$\rho_S = a_S + b_S S$  and  $\rho_T = a_T + b_T T$  where  $a$  and  $b$  are the best-fit parameters. The rms deviations of  $\rho - \rho_S$  and  $\rho - \rho_T$  are computed and are non-dimensionalized by the rms Thorpe fluctuation  $[1/n \sum_{i=1}^n (\rho - \hat{\rho})^2]^{1/2}$ . The resultant ratios are denoted  $\xi_S$  and  $\xi_T$  respectively and are positive definite quantities that approach 0 for tight T-S relationships. The tightness of the density curve is taken as the maximum of the two, i.e.  $\xi = \max(\xi_S, \xi_T)$ . Overturns are determined real if  $\xi$  is below some critical value. The critical value of 0.5 determined by Galbraith and Kelley (1996) is used here. Applying the water-mass test decreases the total amount of overturns detected to 305.

Figure 3.2 shows an overturn that passes both the run-length test and the water-mass test. The density inversion shows a nice z-shape with a region of heavier water above lighter water. The T-S relationship is quite tight with  $\xi = 0.117$ . Figure 3.3 shows an example of an overturn which passes the run-length test, but fails the water-mass test. There are many loops present and locations where the T-S diagram deviate from a straight line. This is quantified with a tightness of  $\xi = 0.603$ .

### 3.4 Computing Dissipation Rates

The minimum detectable dissipation rate can be calculated from (3.10) using values  $\delta z = 0.15$  m and  $N = 0.02$  s<sup>-1</sup> for the vertical resolution and buoyancy frequency respectively. This gives the minimum  $\epsilon$  to be  $1.5 \times 10^{-6}$  W/kg, which is roughly three times smaller than the mean dissipation rate of  $4 \times 10^{-6}$  W/kg measured by Bourgault et al. (2008) in this region. The dissipation rate varies significantly in this region

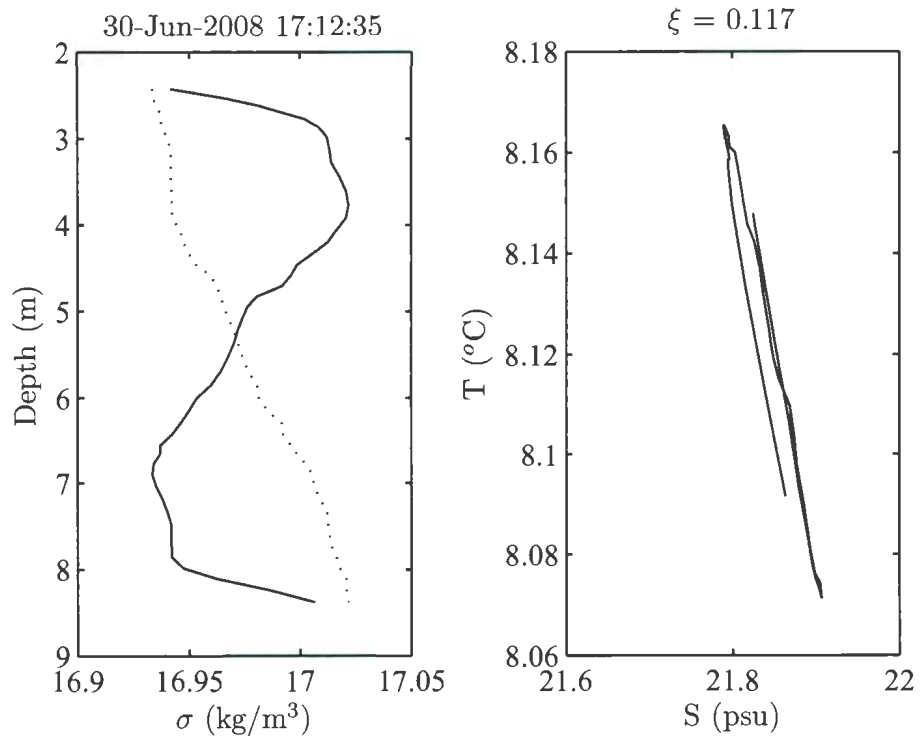


Figure 3.2: An overturn which passes both the run-length test and water-mass test. The solid line denotes the raw ctd profile and the dotted line is the profile sorted to be gravitationally stable.

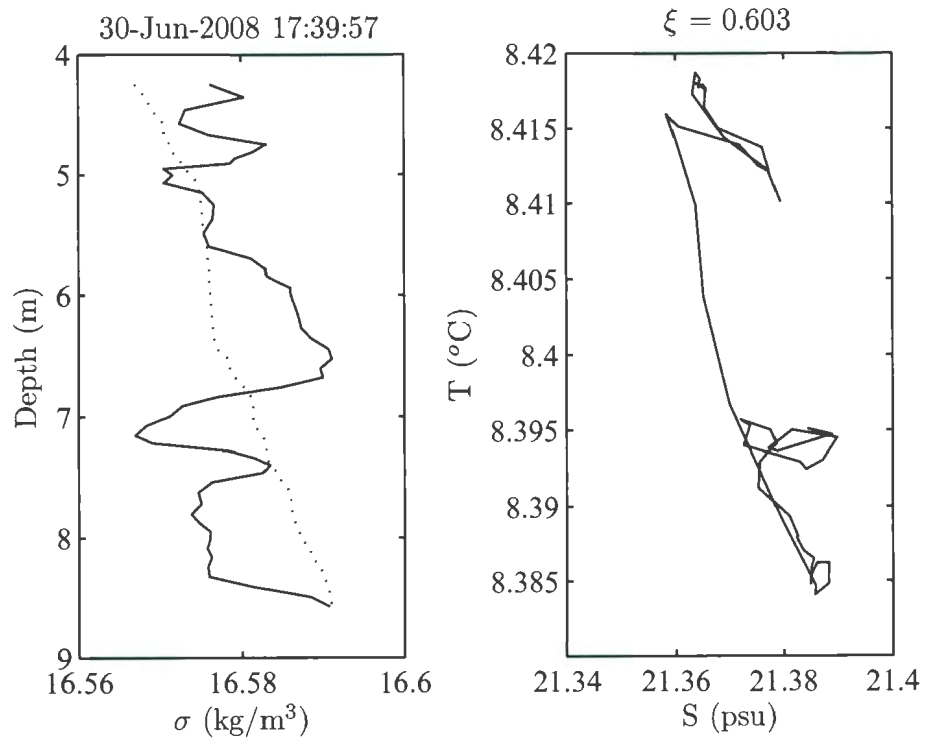


Figure 3.3: An overturn which passes the run-length test but not the water-mass test. The solid line denotes the raw ctd profile and the dotted line is the profile sorted to be gravitationally stable.

( $4 \times 10^{-8}, 2 \times 10^{-5}$  W/kg, Bourgault et al. (2008)) so there is expected to be some mixing events that will be below the resolution limit.

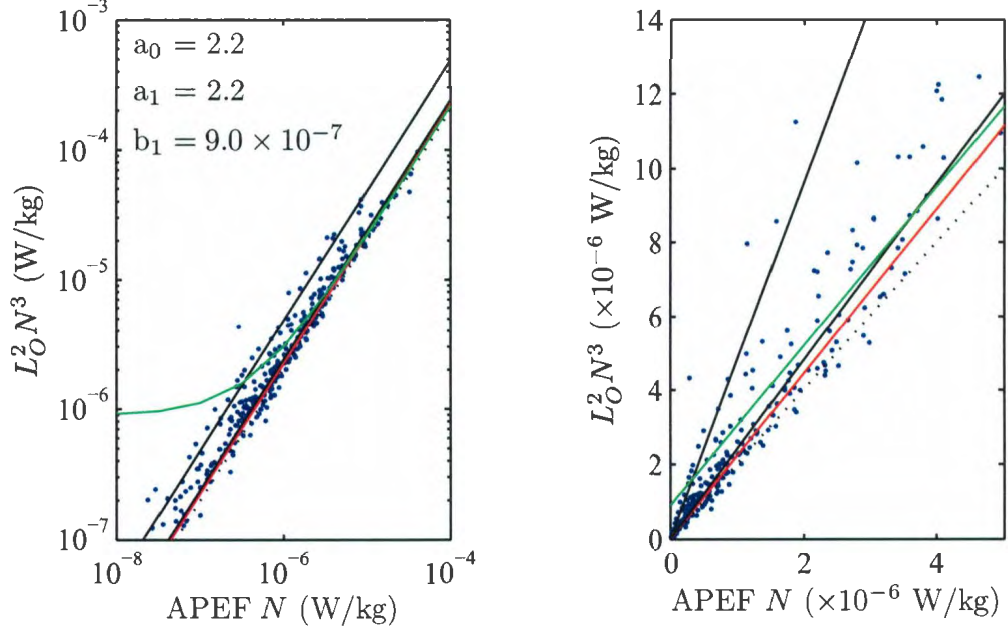


Figure 3.4: Linear fit of  $L_O^2 N^3$  vs APEF  $N$ . The solid lines denote the range for  $a$  of 2.4-4.8. The left panel is the log scale and the right panel is the linear scale. The red line is the linear fit forced through zero with slope  $a_0$  and the green line is the linear fit with  $a_1$  and  $b_1$  as the slope and intercept respectively. The dotted black line shows the slope for  $a = 2$ .

Using (3.1) and (3.3) and the relation  $L_O \sim L_T$ , an empirical value for  $a$  can be determined. Figure 3.4 shows a scatter plot of  $L_O^2 N^3$  vs APEF  $N$ . Two slightly different fits were performed: one using a standard least-squares fit i.e.  $L_O^2 N^3 = a_1 \text{ APEF } N + b_1$  and another forcing the intercept to be zero  $L_O^2 N^3 = a_0 \text{ APEF } N$ .

Both fits found the slope to be identical,  $a = 2.2$ , which is similar to previous studies (Crawford 1986).

Of the 305  $\epsilon$  values calculated, 47% of them lie within the 2.4-4.8 range for  $a$  found by Crawford (1986) (Figure 3.4, solid black lines). Galbraith and Kelley (1996) showed for a z-shaped overturn in a linearly stratified fluid, and assuming as we did that  $L_O \sim L_T$ , that  $\epsilon \sim 2 \text{ APEF } N$ . In fact, 33% of the data points lie within a range for  $a$  of 2-2.4. So decreasing the lower limit of  $a$  to two would account for 80% of the  $\epsilon$  values. All  $\epsilon$  values calculated with (3.3) will use 2.2 for  $a$  and will be denoted  $\epsilon_A$ . Dissipation rates computed with (3.1) will be denoted as  $\epsilon_L$ .

Dissipation rates as a function of tidal phase are shown in Figure 3.5. The dissipation rates are summed into 30 minute bins and calculated for both (3.3) and (3.1). At first glance there seems to be little difference between  $\epsilon_A$  and  $\epsilon_L$ , which is encouraging as it allows the two methods to be used interchangeably. This will be explored in more detail in section 3.5. There is a lot of variability in  $\epsilon$  from tide to tide for each method and with just five incomplete flood tides it is difficult to discern any clear pattern with regards to tidal phase. This will also be investigated further in section 3.5.

### 3.5 Statistical Distribution

To help determine the tidal variation of  $\epsilon$ , each overturn is sorted by tidal phase. Figure 3.6 shows values for  $\epsilon_L$  and  $\epsilon_A$  for every overturn which passed the run-length and water-mass tests. Of the total 305 overturns, 179 of  $\epsilon_L$  and 171 of  $\epsilon_A$  are greater than the minimum resolvable  $\epsilon$  of  $1.5 \times 10^{-6} \text{ W/kg}$ . However, equation (3.10) is very

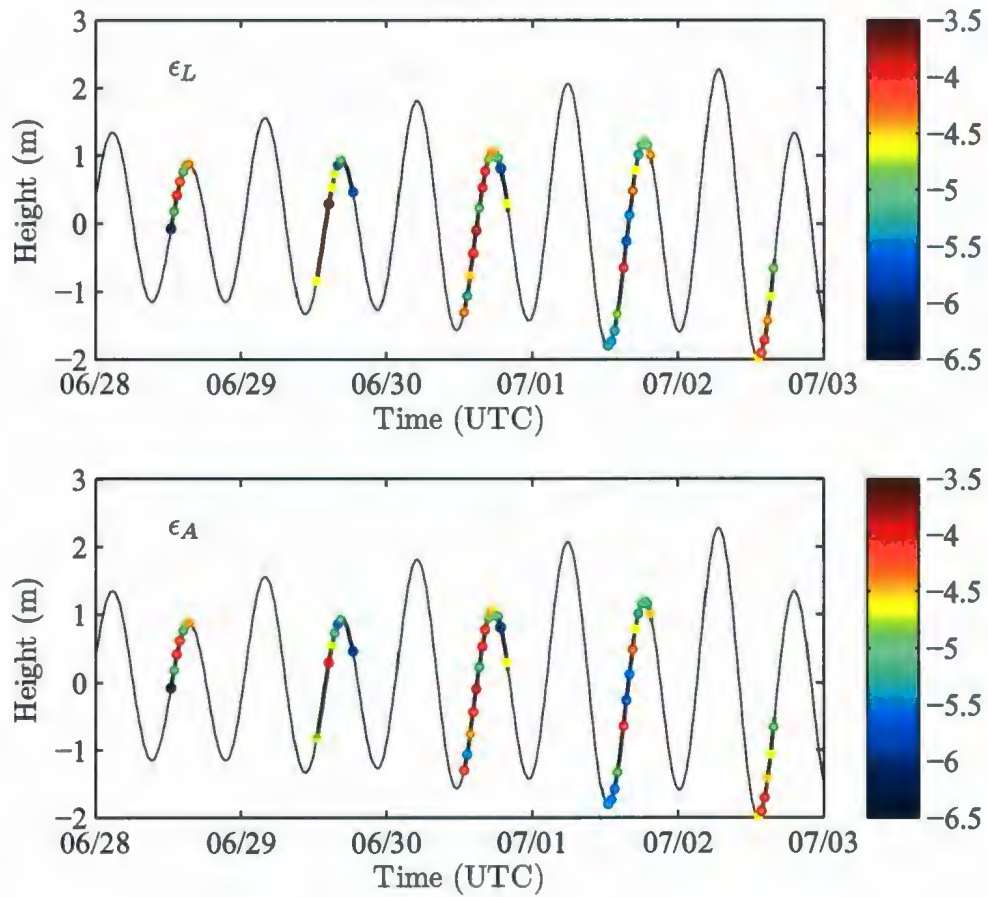


Figure 3.5: Measured values of  $\epsilon$  as a function of tidal phase. The dark black lines denote the times where measurements are available. The values are summed into 30 minute bins. The colour scale is in  $\log(W/kg)$ .

sensitive to the choices of  $\delta z$  and  $N$  which will vary from profile to profile so this additional criterion won't be applied to filter overturns that pass the run-length and water-mass tests.

Without direct measurements of turbulence, it is impossible to determine whether  $\epsilon_L$  or  $\epsilon_A$  should be used, so we will use  $\epsilon_L$  for all subsequent calculations of  $\epsilon$ . The mean and median value of  $\epsilon_L/\epsilon_A$  are 1.3 and 1.1 respectively, suggesting that  $\epsilon_L$  gives consistently larger dissipation rates, but that the distribution is centered much closer to unity. Subsequent calculations will only involve  $\epsilon_L$  as the difference between the two will be much smaller than the range of  $\epsilon$ , which varies by several orders of magnitude.

To determine the statistical nature of the overturns, it is important to know how the overturns are distributed as a function of tidal phase. Figure 3.7 shows the number of overturns and the total number of downcasts present in each 30 minute bin as a function of hours after low water. There are a lot of overturns detected between LW + 1 hrs and LW + 3 hrs that have a dissipation rate less than that computed with (3.10) of  $1.5 \times 10^{-6}$  W/kg. This coincides with the peak period of shoaling internal waves (Bourgault and Kelley 2003; Bourgault et al. 2005) for this region.

Common overturning parameters, i.e. Thorpe scale, overturn height, and available potential energy, are shown in Figure 3.8. These parameters don't appear to vary significantly over the phase of the tide. There is less variation between LW + 3 hrs and LW + 4 hrs in the Thorpe Scale, but this is minimal. There are overturn heights that are less than (3.6) which assumes a constant  $\delta z$ . This is clearly not the case for all the downcasts. For an overturn to pass a run-length test of 7 points there would

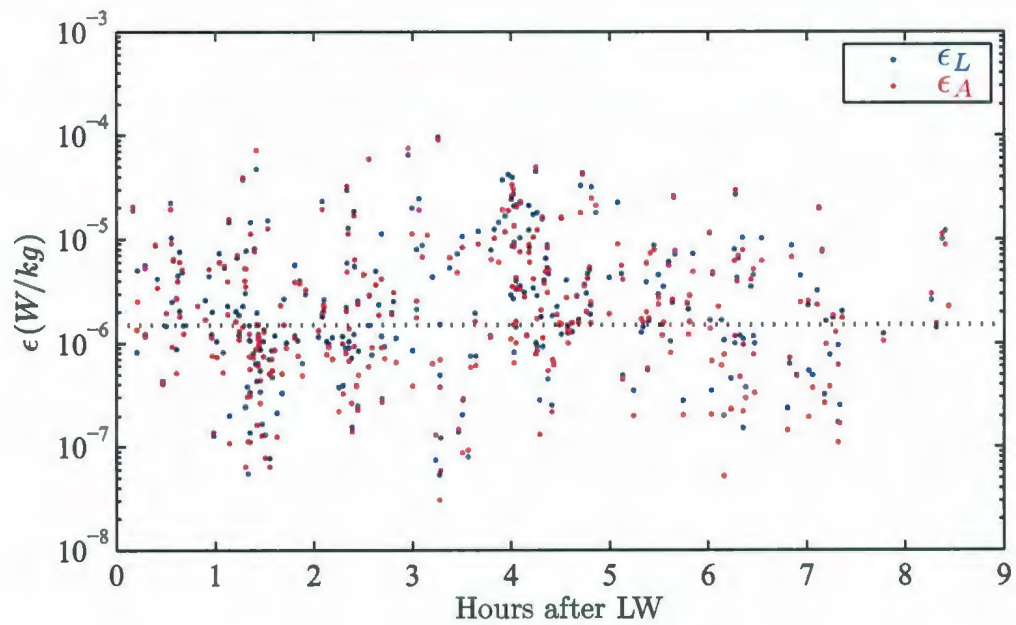


Figure 3.6: Estimated dissipation rate as a function of hours after LW. The black dotted line denotes the minimum  $\epsilon$  resolution of  $1.5 \times 10^{-6} \text{ W/kg}$ . The data is not averaged over time.

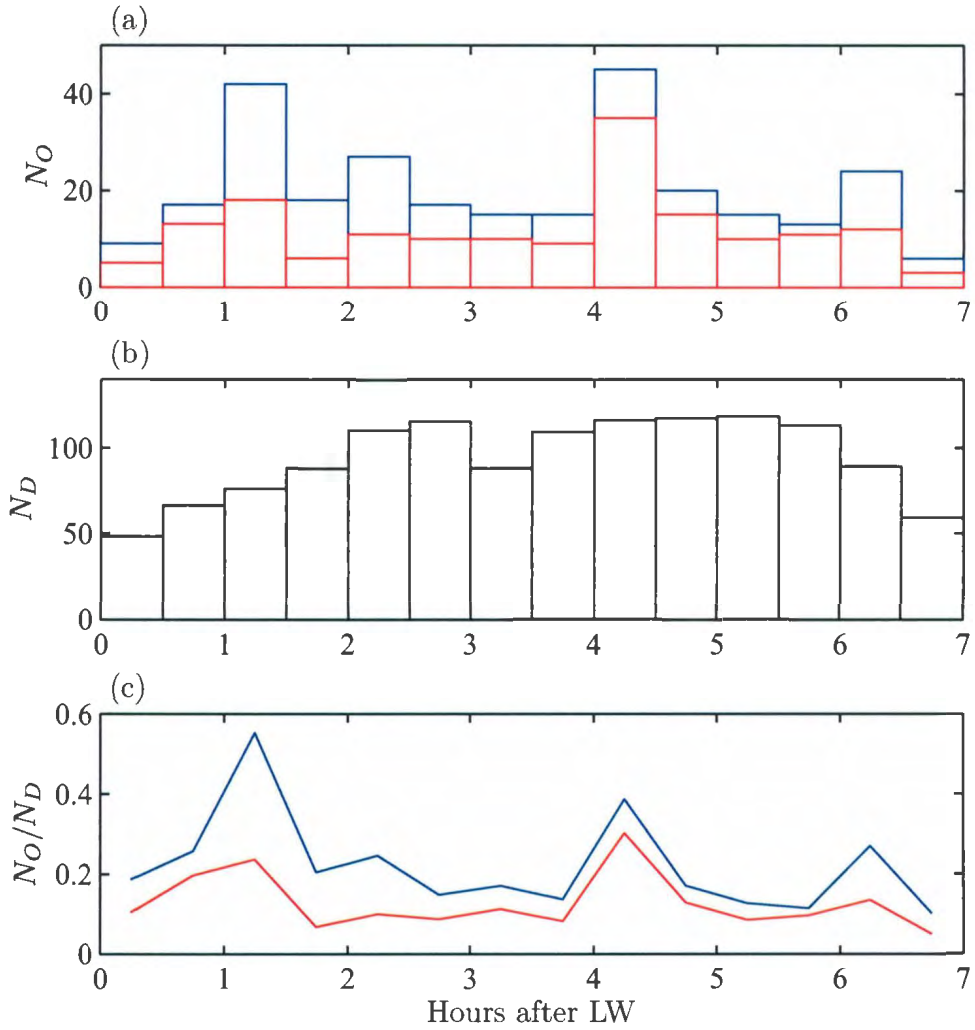


Figure 3.7: The top panel is a histogram of the number of overturns  $N_O$  and the middle panel is the total number of downcasts  $N_D$  for each 30 minute bin respectively. Blue denotes all the overturns and red denotes just those where  $\epsilon > 1.5 \times 10^{-6}$  W/kg. The bottom panel shows the ratio  $N_O/N_D$ . There can be more than one overturn detected per downcast so it is possible for this ratio to exceed one.

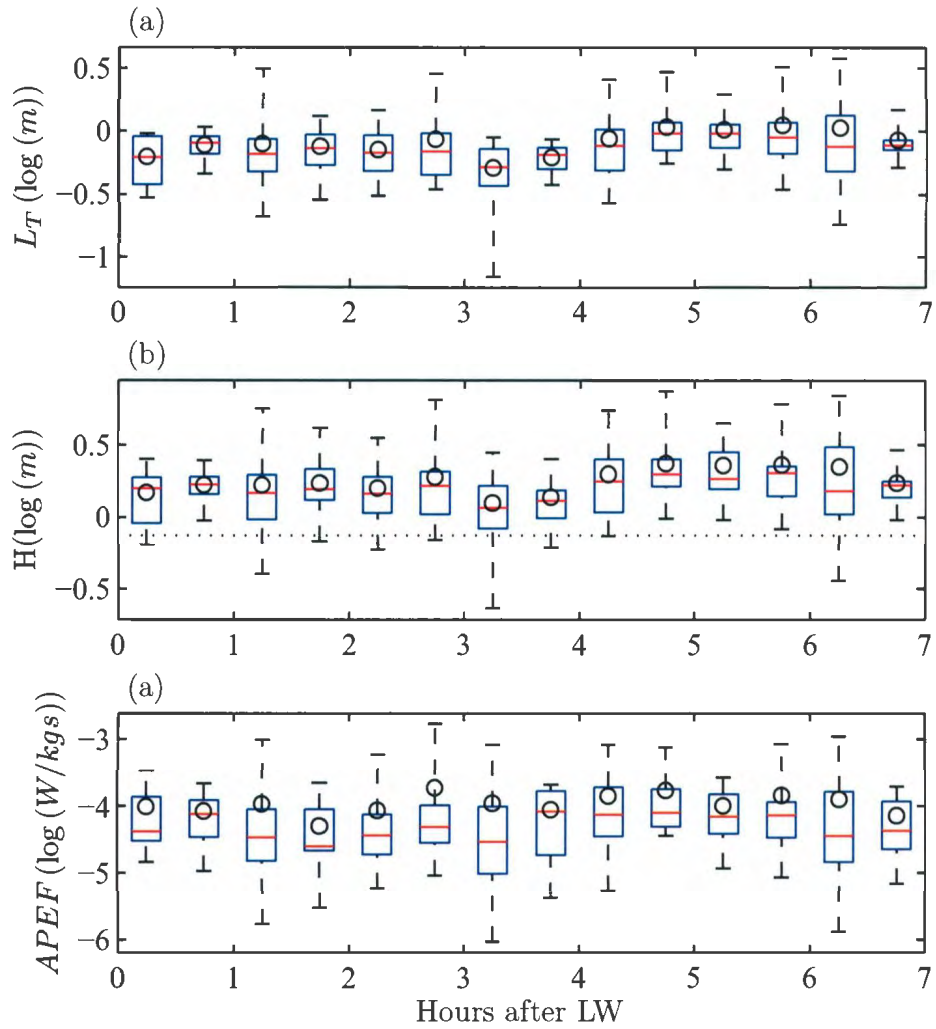


Figure 3.8: Box and whisker plots of overturn statistics. The top panel shows the Thorpe Scale distribution for each 30 minute bin, the middle panel is the overturn height, and the lower panel shows the available potential energy. The minimum overturn height from (3.6) assuming  $\delta z = 0.15$  m is shown with the black dotted line. The red line denotes the median value, the black circle denotes the mean, the blue box encases the data between the 25<sup>th</sup> and the 75<sup>th</sup> percentile, and the whiskers go to the outliers.

need to be a minimum of 14 measurements to detect a complete overturn. This would give a minimum  $\delta z = 0.05$  m for an overturn height of 0.75 m.

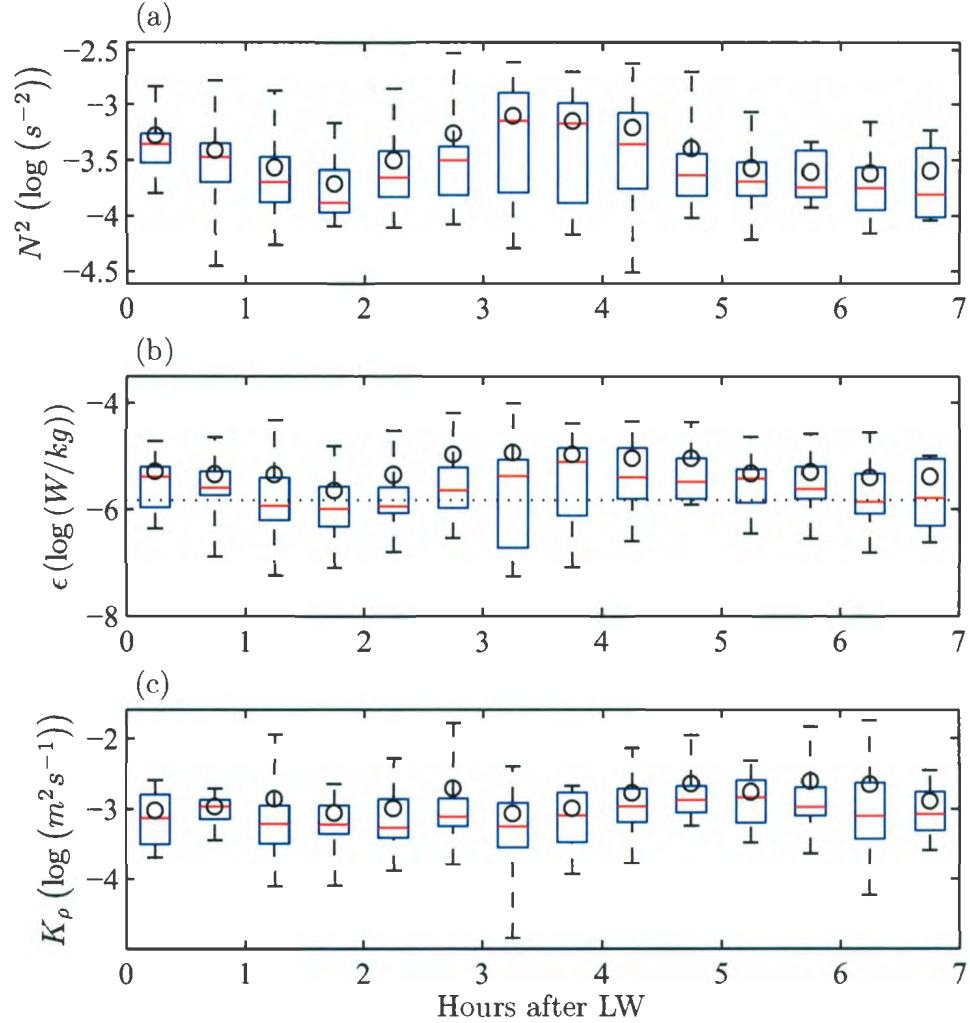


Figure 3.9: Box and whisker plots of turbulent properties. The red line denotes the median value, the black circle denotes the mean, the blue box encases the data between the 25<sup>th</sup> and the 75<sup>th</sup> percentile, and the whiskers go to the outliers. The dotted line on the middle panel denotes the theoretical minimum  $\epsilon$  of  $1.5 \times 10^{-6}$  W/kg.

Turbulent properties associated with density overturns are shown in Figure 3.9. The mean and median stratification, shown in Figure 3.9(a), show an increase in stratification during the peak tidal current, i.e. LW + 3.5 hrs, compared with other phases of the flood tide. Figure 3.9(a) also shows a greater variation in  $N^2$  corresponding with the same phase of the tide as can be seen by the greater extent the 25<sup>th</sup> and 75<sup>TH</sup> edges of the boxplot extend. This greater variation is also seen in the dissipation during the same phase (Figure 3.9(b)), which follows a similar pattern to  $N^2$ . There are many dissipation events that are below the mean value calculated from (3.10) of  $1.5 \times 10^{-7}$  W/kg during all phases of the tide. This is most obvious between LW + 1 hrs and LW + 2.5 hrs where over 50% of the detected dissipation is below this threshold as shown in Figure 3.7(b).

All of the measured dissipation estimates are within  $10^{-7}$  and  $10^{-4}$  W/kg, consistent with the findings of Bourgault et al. (2008). The median and mean value over all times are  $2.3 \times 10^{-6}$  W/kg and  $6.4 \times 10^{-6}$  W/kg respectively, which is very similar to the mean value determined by Bourgault et al. (2008) of  $4 \times 10^{-6}$  W/kg from directly measuring the turbulence with a microstructure profiler in the same region. It is expected that the mean calculated in this study will be greater as the smaller overturns can't be detected with this method and require direct microstructure measurements that were obtained by Bourgault et al. (2008).

The turbulent eddy diffusivity,  $K_\rho$ , is calculated with  $K_\rho = \Gamma\epsilon/N^2$  (Moum et al. 2003; Klymak and Gregg 2004) where  $\Gamma$  is the mixing efficiency. A standard value for  $\Gamma$  is 0.2 (Moum et al. 2003; Klymak and Gregg 2004), but here a value of 0.1 that was calculated in this region from the energy budget of shoaling internal waves (Mirshak

2008). Calculations from the internal wave power, Mirshak (2008) found  $K_\rho$  to be on the order of  $10^{-3}$  m<sup>2</sup>/s during the flood tide. Indeed most of the  $K_\rho$  estimates shown in Figure 3.9(c) are within  $10^{-4}$  and  $10^{-2}$  m<sup>2</sup>/s for all the phases of the flood tide with a median and mean value of  $8.7 \times 10^{-4}$  m<sup>2</sup>/s and  $1.5 \times 10^{-3}$  m<sup>2</sup>/s respectively. Mirshak (2008) found  $K_\rho$  to vary by a factor of 2, but his values are averaged into 1/8 of a tidal period ( $\approx 94$  min), thus averaging out the larger range recorded here with 30 minute temporal bins. Mirshak (2008) also found a slight increase in  $K_\rho$  during peak tidal currents, but this is not observed here with this data set. This is most likely due to their method of computing  $K_\rho$ , which is from the energy budget of ISWs while this method looks at any overturn and they may not necessarily be induced by ISWs.

## Chapter 4

# Field Observations: Shoaling

## Events

Shoaling internal waves are a prevalent feature in this region of the St. Lawrence estuary and are predominantly observed between LW + 1 hrs and LW + 3 hrs with strong and highly variable dissipation rates (Bourgault and Kelley 2003; Bourgault et al. 2005; Bourgault et al. 2007; Bourgault et al. 2008). Two distinct shoaling events are presented in this chapter. The first is a clear visualization of a shoaling internal wavetrain onto the beach at Ile-aux-Lièvres Island. The wavetrain is visualized approaching the shore from multiple echosounder transects onto and off the shore beside the *Lampsilis*. The density and current structure of the shoaling waves are observed from the anchored *Lampsilis*. The second event is a large turbulent front that is visualized offshore as it approaches Ile-aux-Lièvres Island. The nature of this event is more complicated and some of the current and density structure is explained from measurements aboard the *Lampsilis* as it and successive waves pass

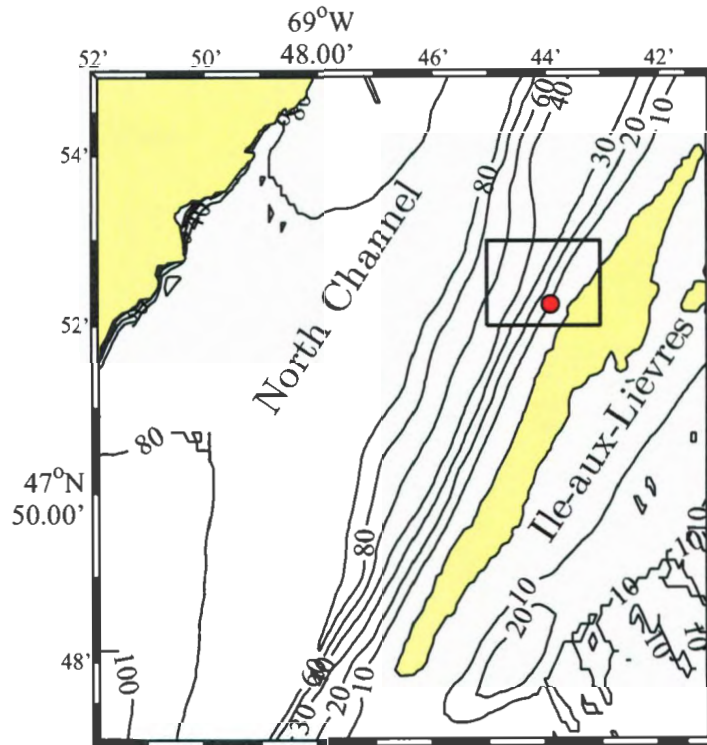


Figure 4.1: The region of ISWs the St. Lawrence Estuary. The red dot denotes the location of the *Lamprolaima*. The black box denotes the inset for all subsequent plots of the echosounder transects.

by. The shoaling waves were all observed within the region identified by the inset box of Figure 4.1.

## 4.1 Internal Solitary Wave Sequence

Between 14:10 and 14:30 UTC ( $\approx$  LW + 4 hrs) on June 29, 2008 the echosounder was able to visualize a series of internal solitary waves (ISWs) (Figure 4.3). The transect locations for the echosounder are shown in Figure 4.2. This sequence of

ISWs occurs just after the expected period of shoaling ISWs between LW + 1 hrs and LW + 3 hrs (Bourgault and Kelley 2003), but corresponds to a time of strong turbulent dissipation rates for this study (Figure 3.9). The propagating waves appear as high acoustic backscatter from the high turbulence associated with propagating ISWs (Moum et al. 2003). Figure 4.3(a) shows the first approaching wave at 14:14 UTC and the subsequent offshore ISWs as they propagate towards the coast. The successive wave pattern can be observed in panels a to c as waves of depression from the pycnocline at  $\approx 4$  m with an amplitude of  $\approx 6$  m. This depression extends the bottom of the ISWs to 10 m depth, which is slightly shallower than the depth at the moored location of the *Lampsilis* of 14 m during this event. Therefore, no boluses are expected to be observed at this location unlike the observations of Bourgault et al. (2007) and Bourgault et al. (2008).

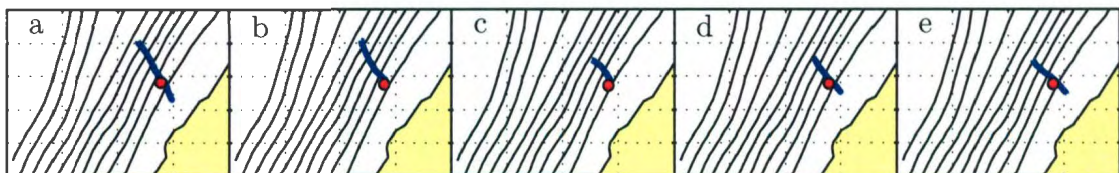


Figure 4.2: Location of each of the echosounder transects associated with Figure 4.3 with the location of the *Lampsilis* denoted by the red dot. The depth contours denote every 5 m depth interval from 5 to 50 m.

Instability in a localized shear layer, also known as Kelvin-Helmholtz (KH) instability, can be observed in Figure 4.3(c) ( 12 m depth, 14:24 UTC) as rollups or billows. Although these billows have been observed in laboratory experiments (Koop

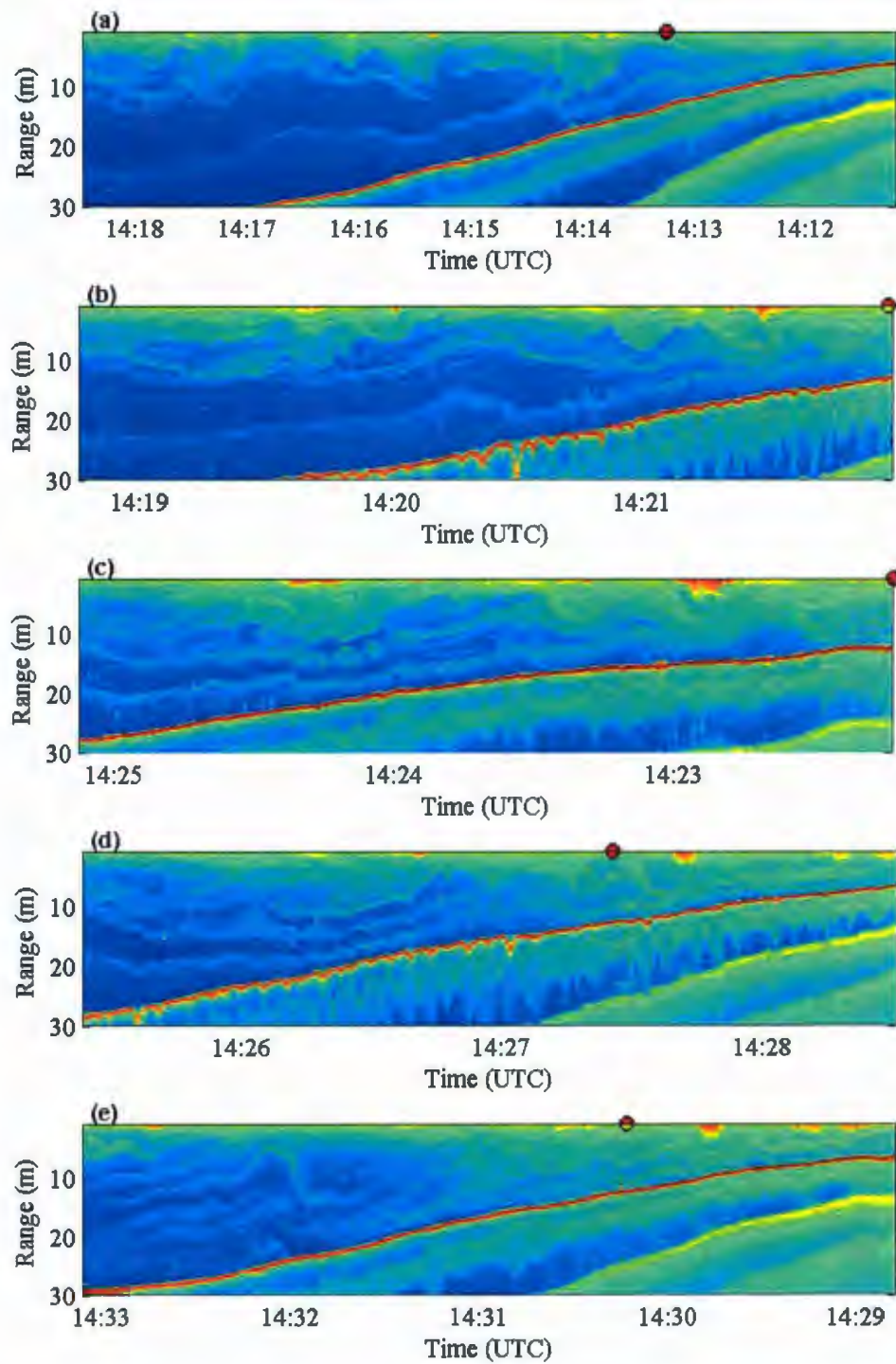


Figure 4.3: Echosounder images of an approaching internal wave. The red dots denote where the transects pass nearest to the Lampsilis.

and Browand 1979) and numerical simulations (Smyth and Moum 2000; Smyth et al. 2001) they are rarely resolved clearly in field measurements (Moum et al. 2003). Unfortunately there are no current or density measurements of the KH billows to calculate associated turbulent and mixing parameters.

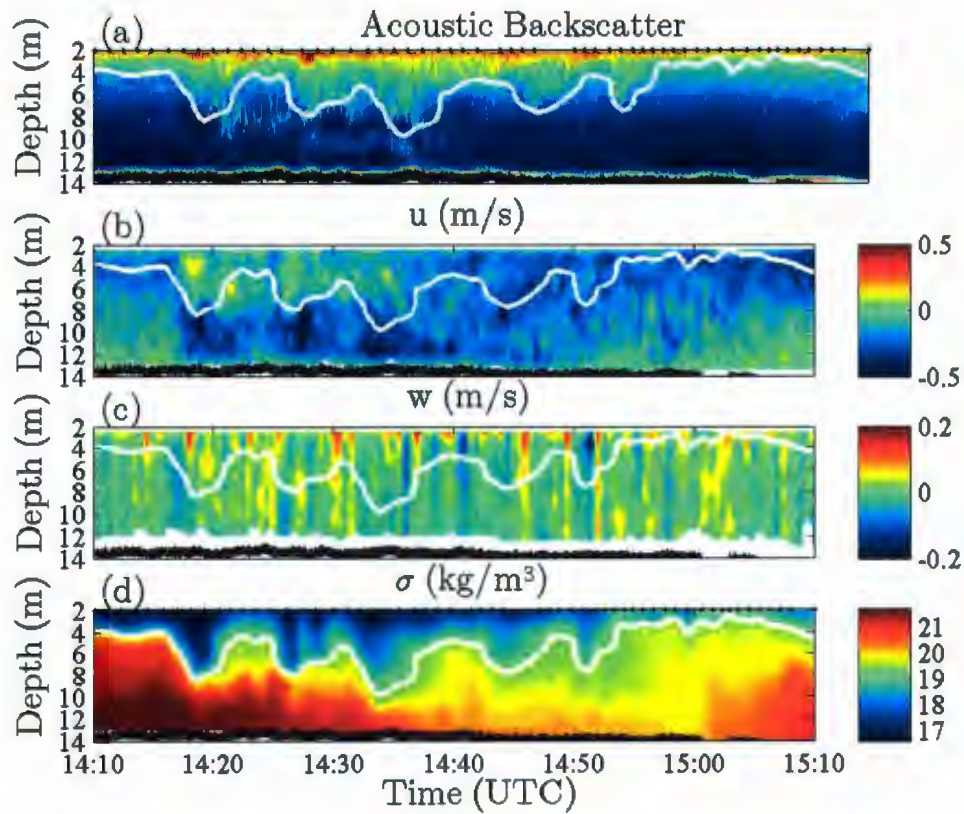


Figure 4.4: ADCP measurements of a shoaling internal wave on June 29, 2009. The black dots along the top are the downcast locations and the white line is the density contour for  $\sigma = 19.4 \text{ kg/m}^3$ .

Velocity profiles and the sampled density field from the anchored *Lampsilis* are shown in Figure 4.4. The pycnocline is initially located at 4 m, but oscillates as

the ISWs pass by the *Lampsilis* (Figure 4.4, white contour line). This motion is also well observed in the acoustic backscatter (Figure 4.4(a)) as regions of high backscatter above the pycnocline. Also, a characteristic of ISWs is the convergence of the onshore velocity,  $u$ , at the front of the wave where downwelling occurs (Figure 4.4(b), 14:17 UTC) and the divergence at the rear due to upwelling at 14:24 UTC (Moum et al. 2003).

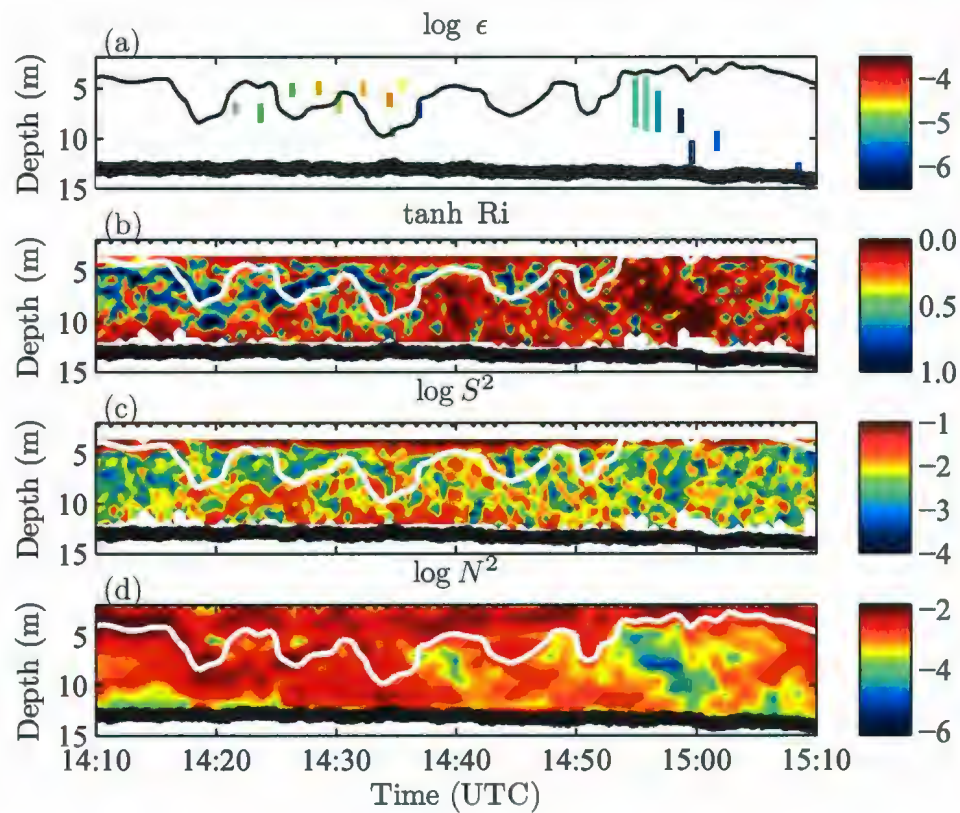


Figure 4.5: Richardson number for a shoaling internal wave on June 29, 2009. The black dots along the top are the downcast locations. The white line is the density contour for  $\sigma = 19.4 \text{ kg/m}^3$ .

After the ISW passes the *Lampsilis*, the pycnocline, corresponding here to  $\sigma = 19.4 \text{ kg/m}^3$ , is no longer easily observed in the backscatter or in the density field. Could this weaker stratification lead to more overturns detected? Figure 4.5(a) shows overturns detected during the ISW sequence. The colour of each line denotes the turbulent dissipation,  $\epsilon$ , calculated from (3.1) and the depth that each line spans corresponds to the height of the overturn. As the ISWs propagate past the *Lampsilis*, the overturns detected are at the lower limit of the vertical resolution which can be resolved from CTD measurements ( $\sim 1 \text{ m}$ ), but are highly dissipative (between  $10^{-5}$  and  $10^{-4} \text{ W/kg}$ ).

These small overturns don't correspond well with the Richardson number (Figure 4.5(b)) as the Richardson number is calculated for a 2 m scale and doesn't resolve the smaller scale shear and stratification. The hyperbolic tangent of the Richardson number is shown here as it has the limits  $\tanh Ri \approx Ri$  for  $Ri \leq 0.25$  and  $\tanh Ri \rightarrow 1$  as  $Ri \rightarrow \infty$ . The overturns observed after the ISWs pass are much larger in height, 4 to 5 m, and do correspond to low Richardson numbers. These overturns have a much smaller  $\epsilon$ , between  $10^{-6}$  and  $10^{-5} \text{ W/kg}$ , so it appears that there is more dissipation as the ISWs approach and break on the shore.

Figures 4.5(c) and (d) show the shear and buoyancy frequency respectively. These are resolved with a vertical filter that filters out vertical wavelengths less than 2 m. For the mean stratification this resolution is adequate, but it is far too coarse to accurately determine the shear to resolve the Richardson number on the spatial scales of each overturning region. The Richardson number used here is a qualitative tool to help deduce relatively stable patches and relatively unstable patches.

## 4.2 Turbulent Front

A large turbulent patch was observed with the echosounder on 28 June, 2008 (Figure 4.7) with the transect locations shown in Figure 4.6. As in Figure 4.3, there appears to be KH billows as the front approaches the shore (Figure 4.7(a) at 13:03 UTC and Figure 4.7(b) at 13:06 UTC). This does not appear to be an ISW as there is no clear wave of depression in the echosounder images. This front is also at  $\approx$  LW + 4 hrs, which is again just after the expected period of intense ISWs between LW + 1 hrs and LW + 3 hrs (Bourgault and Kelley 2003), but corresponds to a time of high turbulent dissipation rates for this study (Figure 3.9).

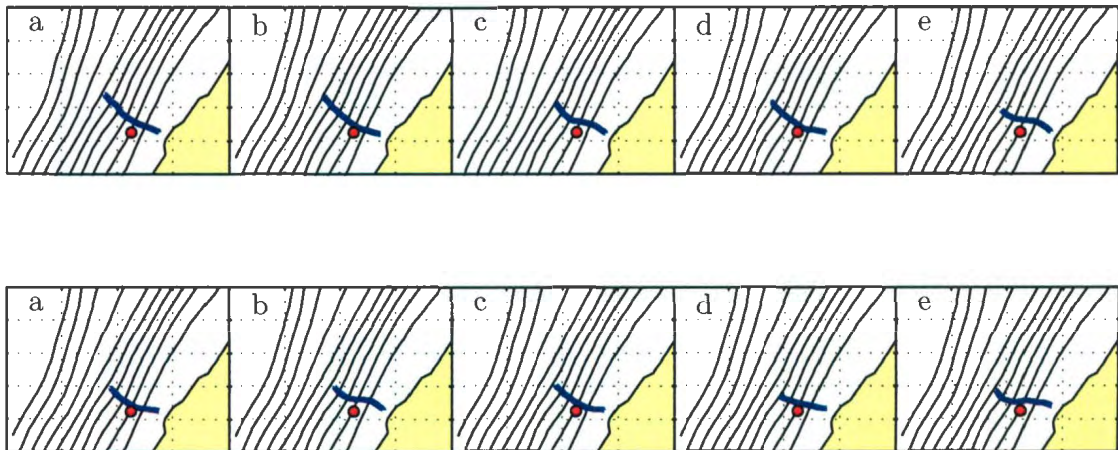


Figure 4.6: Location of each of the echosounder transects associated with Figures 4.7 (top panel) and 4.8 (bottom panel) with the location of the *Lampsilis* denoted by the red dot. The depth contours denote every 5 m depth interval from 5 to 50 m.

The initial patch (Figures 4.7(a) and (b)) show a large thick turbulent feature

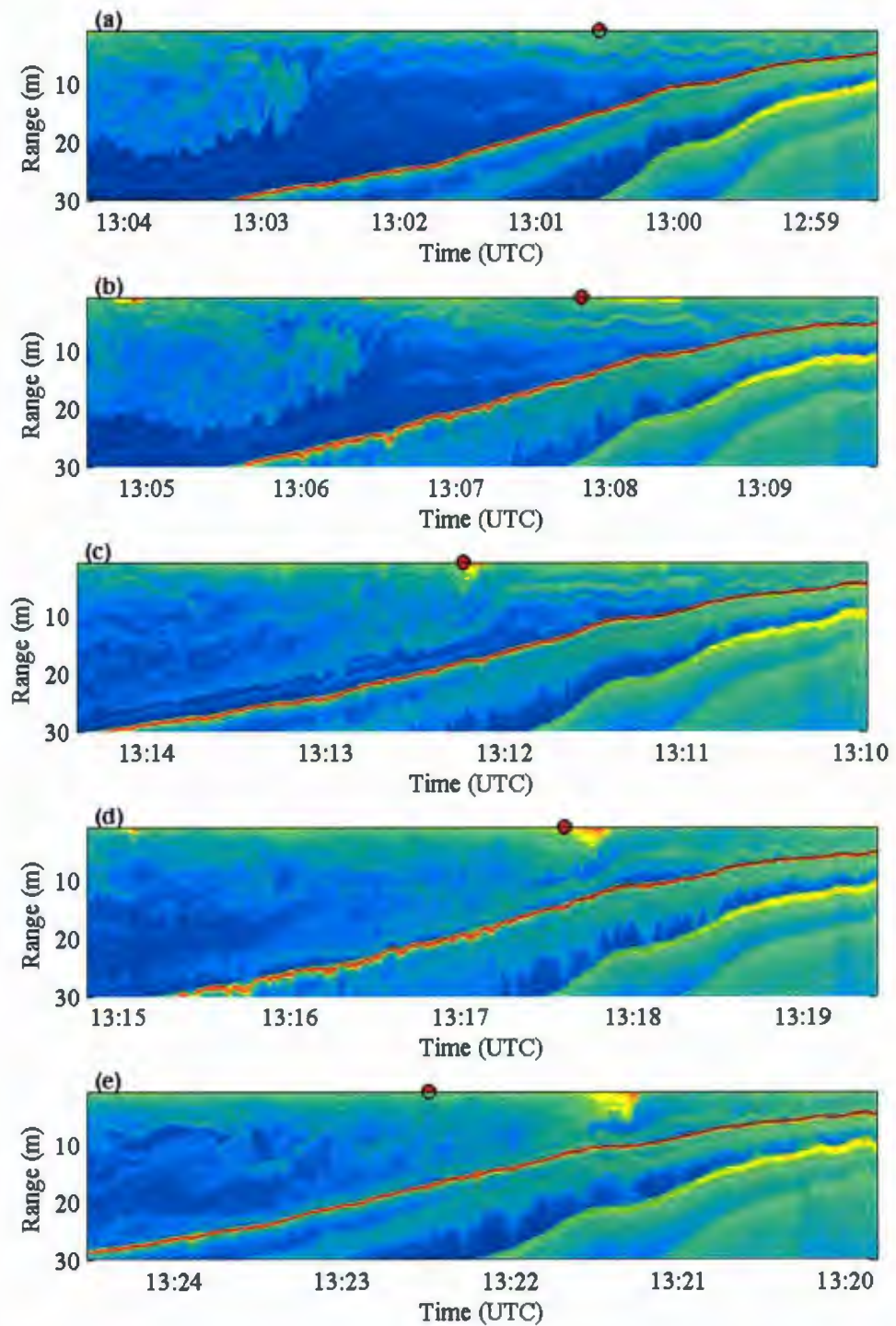


Figure 4.7: Echosounder images of an approaching internal wave. The red dots denote where the transects pass closest to the Lampsilis.

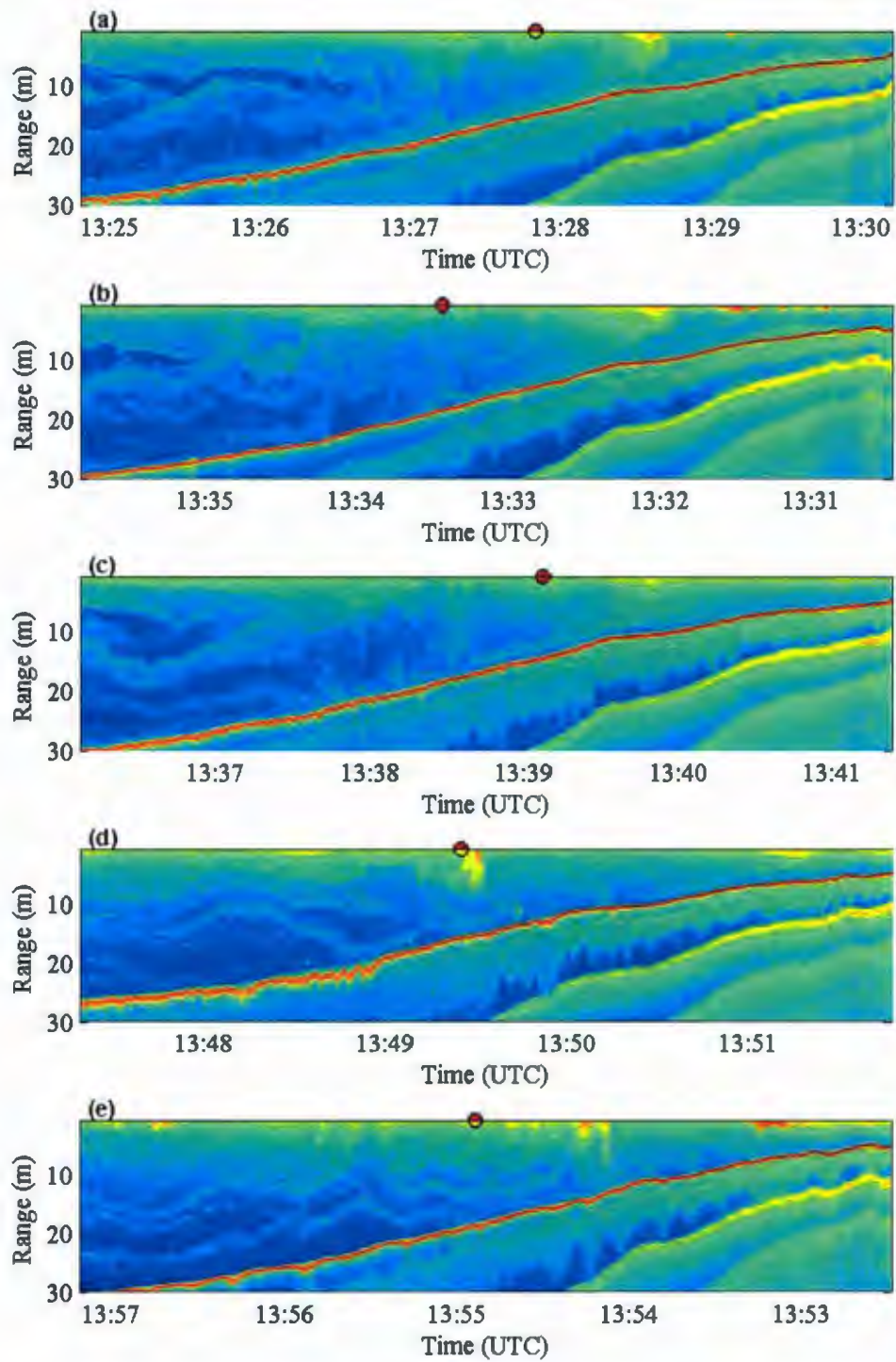


Figure 4.8: More echosounder images of an approaching internal wave. The red dots denote where the transects pass closest to the Lampsilis.

on the order of 10 m approaching the beach. There appears to be Kelvin-Helmholtz billows on the bottom of this patch, suggestive of shear induced turbulence. The pycnocline prior to the approaching feature is at  $\approx 5$  m depth and this quickly gets deformed by the approaching wave with the pycnocline quickly deepening to near the seabed, Figure 4.7(c), and from the *in situ* density measurements (Figure 4.9(b)). After this event the echosounder images appear to show the water column to be highly turbulent with many features shoaling onto the shore, but no easily discernable wave-like features.

Density measurements were collected from the *Lampsilis* during the event, and the interpolated smoothed density field is shown in Figure 4.9(b). The figure shows the pycnocline at  $\approx 4$  m falling to a couple meters above the seabed as the turbulent front passes. As the front passes there are many overturns detected above the pycnocline (Figure 4.9(a)) with magnitudes on the order of  $10^{-5}$  W/kg. As the pycnocline becomes shallower ( $\approx 13:45$  UTC) density inversions appear below the pycnocline and as the pycnocline deepens again ( $\approx 14:00$ ) the inversions begin to appear above it. This suggests that one side of the pycnocline appears to be more turbulent as the front propagates onshore.

Unfortunately, the ADCP doesn't begin recording until 13:40 and was not able to measure the currents associated with this initial turbulent front as it went by the *Lampsilis*. Figure 4.10 shows the current profiles from 13:40 onward. At 13:50 UTC there is a small amplitude ( $\sim 6$  m) ISW near the surface with the characteristic convergence and divergence in the cross-shelf flow (Figure 4.10(b)) corresponding to regions of downwelling and upwelling respectively (Figure 4.10(c)). This ISW is fol-

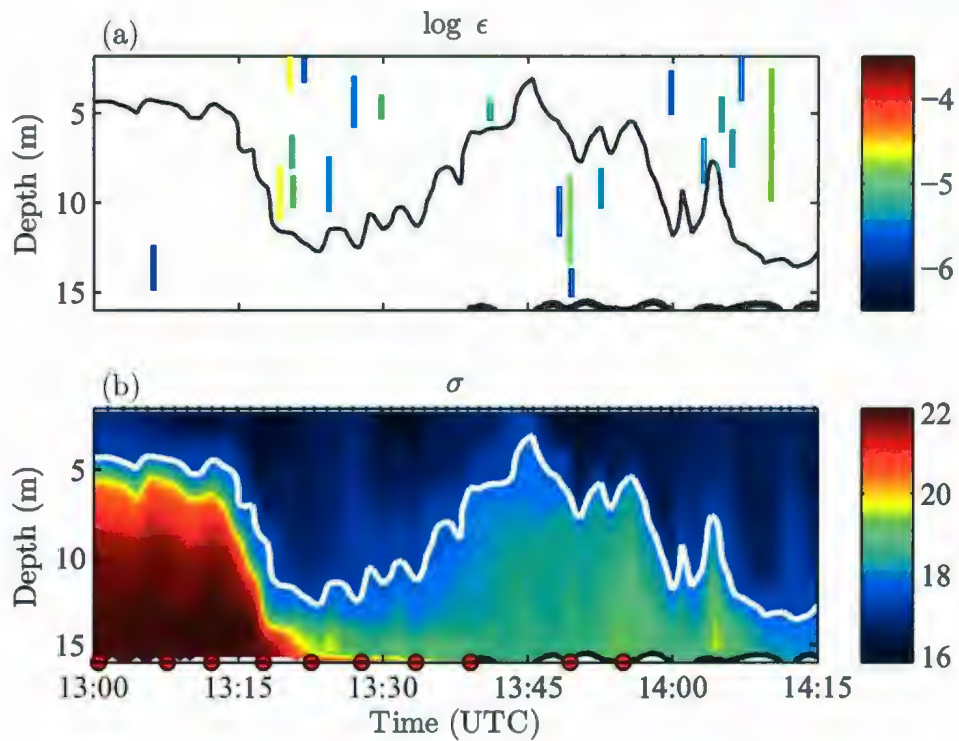


Figure 4.9: The top panel shows the turbulent dissipation rate calculated from over-turns. The colour scale is in  $\text{W/kg}$ . The second panel is the density field for 28 June, 2008 and the colour scale is  $\text{kg/m}^3$ . The black dots along the top are the downcast locations and the large red dots along the bottom are where the echosounder passes closest to the Lampsilis. The white line is  $\sigma = 17.6 \text{ kg/m}^3$ .

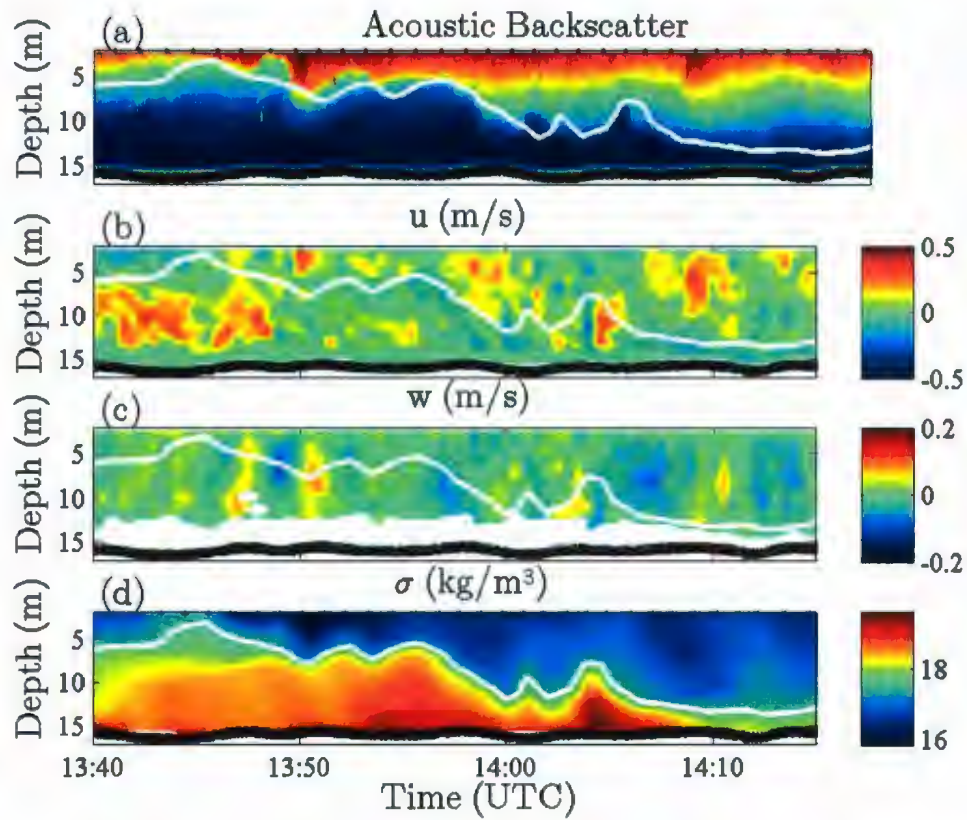


Figure 4.10: ADCP measurements and interpolated CTD density field of a shoaling internal wave on June 28, 2009. The black dots along the top are the downcast locations and the large red dots along the bottom are where the echosounder passes closest to the Lampsilis. The white line shows the density contour for  $\sigma = 17.6$  kg/m<sup>3</sup>.

lowed by a train of smaller waves which occur at the same density contour which is now located at a shallower depth. At 14:00 and 14:05 there appears to be a couple ISWs that also correspond to peaks in the mean density field (Figure 4.10(d)). The velocity structure appears much more complex for these successive waves demonstrating the non-linearity of each wave affecting the upstream condition for the next wave.

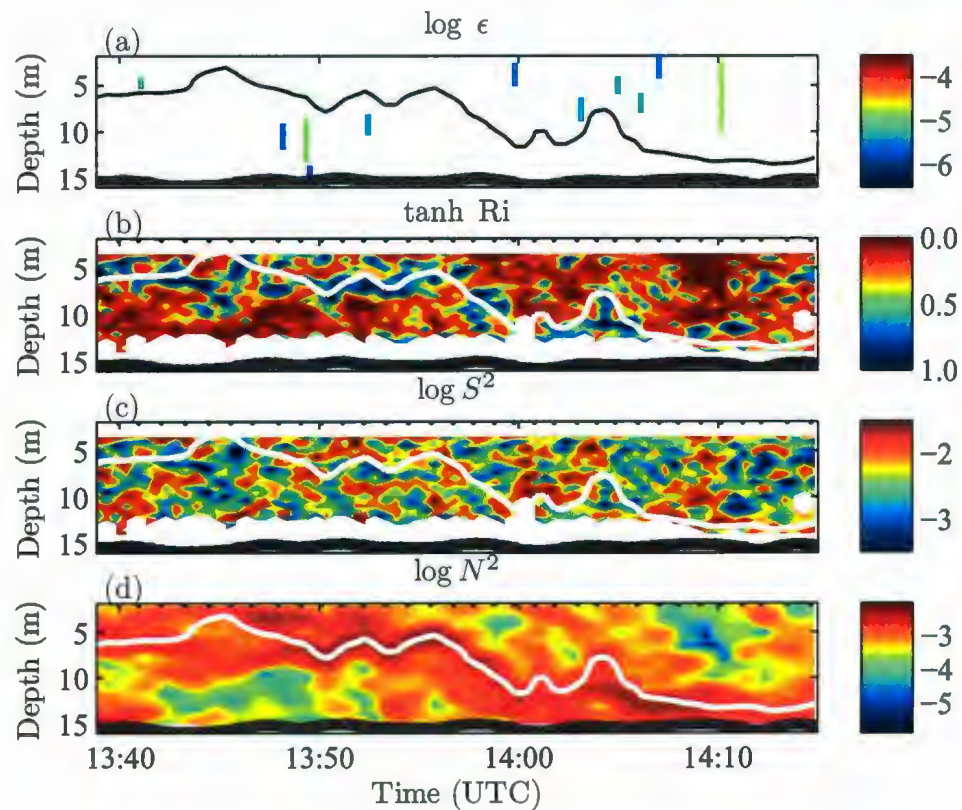


Figure 4.11: Richardson number for a shoaling internal wave on June 29, 2009. The black dots along the top are the downcast locations. The white line shows the density contour for  $\sigma = 17.2 \text{ kg/m}^3$ .

The density overturns for the period where the ADCP is recording are shown in Figure 4.11(a) and are compared with the calculated Richardson number (Figure 4.11(b)) for the tail-end of the turbulent front. The Richardson number is a 2 m scale Richardson number so it is not expected to correspond with the smaller overturns. There are overturns with heights larger than 2 m at 13:50 resulting in a good visual correlation between low Richardson number and overturns detected. This is also the same for the large overturn observed at 14:10. However, for the smaller scale overturns around 14:05 there is less of a clear correlation with low Richardson numbers.

## Chapter 5

# Conclusions and Future Work

### 5.1 Summary

In this thesis, turbulence and mixing parameters were calculated from density inversions obtained from CTD casts for the highly dissipative region near Ile-aux-Lièvres in the St. Lawrence Estuary. A total of 305 overturns were detected over five flood tides using the methodology of Galbraith and Kelley (1996). Common turbulence parameters, including turbulent dissipation rate and eddy diffusivity, are computed for each overturn and binned as a function of tidal phase. Peak values of each turbulent parameter are found at  $\approx LW + 4$  hrs, coinciding with the maximum tidal currents during the flood tide. The mean and range of turbulent dissipation rate and eddy diffusivity are in good agreement with previous studies in the region (Bourgault et al. 2008; Mirshak 2008).

Turbulent dissipation rates were successfully calculated from density overturns observed in CTD casts. The turbulence is large and highly variable with a mean

dissipation rate  $6.4 \times 10^{-6}$  W/kg, which is strikingly similar to the result of Bourgault et al. (2008) of  $4 \times 10^{-6}$  W/kg, and ranges between  $10^{-7}$  and  $10^{-4}$  W/kg. The estimates of Bourgault et al. (2008) are done directly with a microstructure profiler which is able to measure smaller mixing events and hence it is likely that they would measure a lower mean  $\epsilon$  than this study. The mean value varies by an order of magnitude from the minimum of  $10^{-6}$  W/kg at LW + 1.75 hrs to  $10^{-5}$  W/kg at LW + 3.5 hrs (Figure 3.9).

Eddy diffusivities were determined from the turbulent dissipation rate estimates for each overturn. These were much less variable than  $\epsilon$  with a mean and median diffusivity of  $1.5 \times 10^{-3}$  m<sup>2</sup>/s and  $8.7 \times 10^{-4}$  m<sup>2</sup>/s respectively. This is consistent with the results of Mirshak (2008) who found  $K_\rho$  to be on the order of  $10^{-3}$  m<sup>2</sup>/s from the energy conservation of shoaling ISWs.

Two specific shoaling events are presented in detail to analyse the role and timing of overturns with respect to the incoming event. Shear instabilities in the form of KH billows are visualized for both events from echosounder transects. From this study, ISWs create small density inversions (in vertical scale) with high turbulent dissipation rates. This suggests that where these are occurring, the overturn method will be insufficient to accurately estimate much of the turbulent dissipation associated with shoaling ISWs and could partly explain the local minimum detected in the computed  $\epsilon$  during the peak period of ISWs between LW + 1 hrs and LW + 3 hrs. Direct measurements of turbulence would be required to assess whether this is indeed true.

It is very likely that the minimum between the peak ISW period is from a resolution issue and not a physical one. This also helps explain the peak in  $\epsilon$  just after

the peak ISW period, where the shoaling ISWs erode the stratification of the water column which would allow for larger vertical overturns to be detected. This would appear to go against the top panel of Figure 3.9 which shows the distribution of stratification over each overturn. However, the key here is over *each overturn*, so between LW + 1 hrs and LW + 3 hrs only the overturns occurring over less stratified water create large enough overturn patches to be detected here.

## 5.2 Future Work

One clear avenue for future work is to look further into the role of breaking ISWs in the energy budget of the St. Lawrence Estuary. It is unclear from this thesis and previous work (Bourgault and Kelley 2003; Bourgault et al. 2005; Bourgault et al. 2008) how significant breaking ISWs are to the energy budget. In fact, this thesis found higher turbulent dissipation rates not during the period of high ISW activity, but an hour after. Events occurring at LW + 4 hrs do show examples of KH billows, which are observed as a result of shear instabilities. These are only visualized in the echosounder transects and the structure of each is not measured. It is most likely that these shear instabilities are created by the shear induced by the propagating ISW (Moum et al. 2003), but without direct measurements of the billows it is impossible to say with certainty. Perhaps these shear instabilities are a major source of turbulent dissipation in this region? More measurements outside of the surf zone would be required to estimate the turbulent dissipation associated with the KH billows.

The role boluses play in the mixing of the estuary still hasn't been determined. Bourgault et al. (2008) found that boluses were numerous and appeared to bring stability to the surf zone and inhibit turbulent dissipation. These were not prevalent in this data set, but where observed (Figure 4.11) their overturn length scales appear too small to accurately measure the turbulent dissipation rate. Without direct turbulence measurements with a microstructure profiler it is impossible to measure the role that boluses play in mixing.

# Bibliography

- Bourgault, D., M. D. Blokhina, R. Mirshak, and D. E. Kelley (2007). Evolution of a shoaling internal solitary wavetrain. *Geophys. Res. Lett.* *34*, L03601, doi:10.1029/2006GL028462.
- Bourgault, D. and D. E. Kelley (2003). Wave-induced boundary mixing in a partially mixed estuary. *J. Mar. Res.* *61*, 553–576.
- Bourgault, D., D. E. Kelley, and P. S. Galbraith (2005). Interfacial solitary wave run-up in the St. Lawrence Estuary. *J. Mar. Res.* *63*, 1001–1015.
- Bourgault, D., D. E. Kelley, and P. S. Galbraith (2008). Turbulence and boluses on an internal beach. *J. Mar. Res.* *66*, 563–588.
- Bourgault, D., F. J. Saucier, and C. A. Lin (2001). Evolution of a shoaling internal solitary wavetrain. *J. Geophys. Res.* *106*, 9393–9409.
- Canadian Tide and Current Tables (2000). *Vol 3: St. Lawrence and Saguenay Rivers*. Canadian Hydrographic Service, Fisheries and Oceans Canada, Ottawa.
- Crawford, W. R. (1986). A comparison of length scales and decay times of turbulence in stably stratified fluids. *J. Phys. Oceanogr.* *16*, 1847–1854.

- Dickie, L. and L. M. Trites (1983). The Gulf of St. Lawrence. In B. H. Ketchum (Ed.), *Estuaries and Enclosed Seas*, pp. 403–425. Elsevier.
- Dillon, T. M. (1982). Vertical overturns: A comparison of Thorpe and Ozmidov scales. *J. Geophys. Res.* 87, 9601–9613.
- El-Sabah, M. (1988). Physical oceanography of the St. Lawrence Estuary. In B. Kjerfve (Ed.), *Hydrodynamics of Estuaries, 2, Estuarine Case Studies*, pp. 61–78. Boca Raton, FL: CRC Press.
- Ellison, T. H. (1957). Turbulent transport of heat and momentum from an infinite rough plane. *J. Fluid Mech.* 2, 456–466.
- Farmer, D. M. and H. Freeland (1983). The physical oceanography of fjords. *Progr. Oceanogr.* 12, 147–220.
- Galbraith, P. S. and D. E. Kelley (1996). Identifying overturns in CTD profiles. *J. Atmos. Oceanic Technol.* 13, 688–702.
- Gargett, A. and T. Garner (2008). Determining Thorpe scales from ship-lowered CTD density profiles. *J. Atmos. Oceanic Technol.* 25, 1657–1670.
- Goudsmit, G. H., F. Peters, M. Gloor, and A. Wuest (1997). Boundary versus internal mixing in stratified natural waters. *J. Geophys. Res.* 102, 27,903–27,914.
- Helfrich, K. R. (1992). Internal solitary wave breaking and run-up on a uniform slope. *J. Fluid Mech.* 243, 133–154.
- Imberger, J. and P. Hamblin (1982). Dynamics of lakes, reservoirs and cooling ponds. *Ann. Rev. Fluid Mech.* 14, 153–187.

- Imberger, J. and G. N. Ivey (1991). On the nature of turbulence in a stratified fluid. Part II: Application to lakes. *J. Phys. Oceanogr.* 21, 659–680.
- Klymak, J. M. and M. C. Gregg (2004). Tidally generated turbulence over the Knight Inlet sill. *J. Phys. Oceanogr.* 34, 1135–1151.
- Koch, S. E., M. DesJardins, and P. J. Kocin (1983). An interactive Barnes objective map analysis scheme for use with satellite and conventional data. *J. Climate Appl. Meteor.* 22, 1487–1503.
- Koop, C. and F. Browand (1979). Instability and turbulence in a stratified layer with shear. *J. Fluid Mech.* 93, 135–159.
- Kundu, P. K. and I. M. Cohen (2004). *Fluid Mechanics* (Third ed.). San Diego: Elsevier Academic Press. 759 pp.
- Levitus, S. (1982). Climatological atlas of the World Ocean. NOAA Prof. Paper 13, 173pp.
- Lohrmann, A., B. Hackett, and L. P. Røed (1990). High resolution measurements of turbulence, velocity and stress using a pulse-to-pulse coherent sonar. *J. Atmos. Oceanic Technol.* 7, 19–37.
- Lu, Y. and R. G. Lueck (1999a). Using a broadband ADCP in a tidal channel. Part I: Mean flow and shear. *J. Atmos. Oceanic Technol.* 16, 1556–1567.
- Lu, Y. and R. G. Lueck (1999b). Using a broadband ADCP in a tidal channel. Part II: Turbulence. *J. Atmos. Oceanic Technol.* 16, 1568–1579.
- Lueck, R. G. and J. J. Picklo (1990). Thermal inertia of conductivity cells: Obser-

- vations with a Sea-Bird cell. *J. Atmos. Oceanic Technol.* 7, 756 768.
- Miles, J. (1961). On the stability of heterogeneous shear flows. *J. Fluid Mech.* 10, 496 508.
- Mirshak, R. (2008). *Interfacial Internal Waves Impacting Sloped Boundaries*. Ph. D. thesis, Dalhousie University, Halifax, Nova Scotia, Canada.
- Morrison, J., R. Andersen, N. Larsen, E. D'Asario, and T. Boyd (1994). The correction for thermal-lag effects in Sea-Bird CTD data. *J. Phys. Oceanogr.* 11, 1151 1164.
- Moum, J. N., D. M. Farmer, W. D. Smyth, L. Armi, and S. Vagle (2003). Structure and generation of turbulence at interfaces strained by internal solitary waves propagating shoreward over the continental shelf. *J. Phys. Oceanogr.* 33, 2093 2112.
- Munk, W. and C. Wunsch (1998). Abyssal recipes II: energetics of tidal and wind mixing. *Deep-Sea Res.* 45, 1977 2010.
- Munk, W. H. (1966). Abyssal recipes. *Deep-Sea Res.* 13, 707 730.
- Osborn, T. R. (1980). Estimates of the local rate of vertical diffusion from dissipation measurements. *J. Phys. Oceanogr.* 10, 83 89.
- Ozmidov, R. V. (1965). On the turbulent exchange in a stably stratified ocean. *Acad. Sci. USSR Atmos. Ocean Phys.* 1, 853 860.
- Peters, H. (1997). Observations of stratified turbulent mixing in an estuary: neap-to-spring variations during high river flow. *Est. Coastal Shelf Sci.* 45, 69 88.

- Peters, H., M. C. Gregg, and J. M. Toole (1988). On the parameterization of equatorial turbulence. *J. Geophys. Res.* 93, 1199–1218.
- Reid, S. J. (1977). Circulation and mixing in the St. Lawrence Estuary near Ilet Rouge. Technical report, Bedford Inst. Oceanogr. Tech. Report Series/BI-R-77.
- Sandstrom, H., J. A. Elliott, and N. A. Cochrane (1989). Observing groups of solitary internal waves and turbulence with BATFISH and echo-sounder. *J. Phys. Oceanogr.* 19, 987–997.
- Sandstrom, H. and N. S. Oakey (1995). Dissipation in internal tides and solitary waves. *J. Phys. Oceanogr.* 25, 604–614.
- Sea-Bird Electronics (2009). SBEDataProcessing\_7.18d.pdf . Available online at <ftp://ftp.halcyon.com/pub/seabird/OUT/Seasoft-Win32/SBEDataProcessing/>.
- Smyth, W. D. and J. N. Moum (2000). Length scales of turbulence in stably stratified mixed layers. *Phys. Fluids* 12, 1327–1342.
- Smyth, W. D., J. N. Moum, and D. R. Caldwell (2001). The efficiency of mixing in turbulent patches: Inferences from direct simulations and microstructure observations. *J. Phys. Oceanogr.* 31, 1969–1992.
- Stansfield, K., C. Garrett, and R. Dewey (2001). The probability distribution of the Thorpe displacement within overturns in Juan de Fuca Strait. *J. Phys. Oceanogr.* 31, 3421–3434.
- Stigebrandt, A. (1979). Observational evidence for vertical diffusion driven by in-

- ternal waves of tidal origin in Oslo fjord. *J. Phys. Oceanogr.* 9, 435–441.
- Stigebrandt, A. and J. Aure (1989). Vertical mixing in basin waters of fjords. *J. Phys. Oceanogr.* 19, 917–926.
- Thorpe, S. A. (1977). Turbulence and mixing in a Scottish loch. *Phil. Trans. Roy. Soc. London A* 286, 125–181.
- Thorpe, S. A., P. Hall, and M. White (1990). The variability of mixing on a continental slope. *Proc. R. Soc. Lond. A* 439, 115–130.
- Vlasenko, V. and K. Hutter (2002). Numerical experiments on the breaking of solitary internal waves over a slope-shelf topography. *J. Phys. Oceanogr.* 32, 1779–1793.
- Wallace, B. C. and D. L. Wilkinson (1988). Run-up of internal waves on a gentle slope in a two-layered system. *J. Fluid Mech.* 191, 419–442.
- Wunsch, C. and R. Hendry (1972). Array measurements of the bottom boundary layer and the internal wave field on the continental slope. *Geophys. Fluid Dyn.* 4, 101–145.





